Journal of Sound and Vibration 643 (2026) 119981

Contents lists available at ScienceDirect

Journal of Sound and Vibration

journal homepage: www.elsevier.com/locate/jsvi

Submerged floating tunnels: Nonlinear dynamics of anchoring elements subject to hydrodynamic loads

Stefano Corazza [a,*], Francesco Foti [a], Luca Martinelli [a], Vincent Denoël [b]

[a] Department of Civil and Environmental Engineering, Politecnico di Milano, Piazza Leonardo da Vinci 32, Milano, 20133, Italy
[b] Structural and Stochastic Dynamics, Structural Engineering Division, Université de Liège, Liège, 4000, Belgium

A R T I C L E I N F O

Keywords:
Coupled system
Reduced–order model
Multiple time scales
Submerged floating tunnels
Cable dynamics
Mathieu–Duffing equation
Nonlinear vibrations

A B S T R A C T

Seabed-anchored Submerged Floating Tunnels (SFTs) are interesting modular structures which are deemed to be a valuable option for crossing deep and long waterways. Due to their inherent flexibility, SFTs are prone to the effect of dynamic loads. Among all of them, wave loads are deemed to be the most critical for both serviceability and fatigue life assessments of the SFT, because of its recurrent and cyclic nature. The local hydrodynamic response of the anchoring elements typically entails significant computational burden, making both numerical models and CFD simulations unfeasible solutions for the conceptual design phase of SFTs. In the present work, a reduced-order cross-sectional model of the SFT is formulated, by modeling the submerged tube as a two-dof rigid body and describing the planar motion of the anchoring elements according to the small-sag cable theory, accounting for both geometrical nonlinearities and supports motion. The coupled system of equations of motion is derived, and three different loading conditions are studied. Subsequently, the multiple timescales perturbation method is employed to obtain approximate closed-form solutions for the steady-state vibration amplitude of the tethers. Numerical validation of the sought expressions is then presented, and extensive parametric analyses are carried out, with the final aim of providing a quick and reliable tool to guide the conceptual design phase of SFTs.

1. Introduction

Submerged Floating Tunnels (SFTs), also named Archimedes bridges, are underwater modular structures which are deemed to be a valuable option for crossing deep and long waterways, such as sea straits, fjords, bays and alpine lakes. Even though a first realization is still missing, many preliminary design proposals have been developed, starting from the last decade of the past century [1–6].

SFTs consist of a water immersed tubular structure which is floating at a depth of around 20–50 m, both to ensure an adequate navigation clearance and to avoid excessive water pressure. Depending on the net Buoyancy to Weight Ratio (BWR) – i.e. the ratio between the buoyancy force and the self-weight per unit of length of the tunnel – SFTs are kept fixed in position by a spread system of (a) anchoring elements connected to the seabed (BWR > 1, see Fig. 1) or (b) pontoons floating on the water surface (BWR < 1).

* Corresponding author.
E-mail addresses: stefano.corazza@polimi.it (S. Corazza), francesco.foti@polimi.it (F. Foti), luca.martinelli@polimi.it (L. Martinelli), v.denoel@uliege.be (V. Denoël).

https://doi.org/10.1016/j.jsv.2026.119981
Received 13 May 2025; Received in revised form 19 June 2026; Accepted 28 June 2026
Available online 29 June 2026

Seabed-anchored SFTs have been recognized as the most promising solution for practical applications, since the presence of floating pontoons increases the visual impact of the SFT, may determine restrictions to the navigation, and makes the structural system more exposed to the combined action of wind and wave loads [7,8].

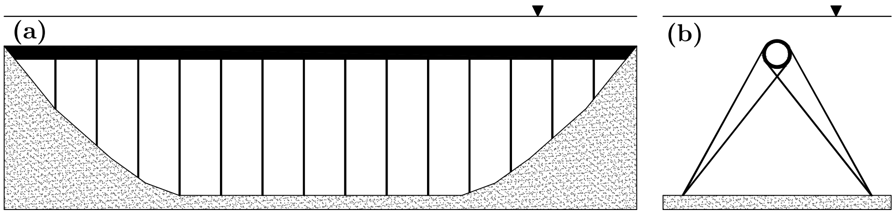

Fig. 1. Schematic of a generic seabed-anchored SFT: longitudinal view (a) and midspan cross-section (b).

A lot of different technological solutions have been proposed for the anchoring elements.

However, they all possess the characteristics of being slender, axially stiff and very flexible in the transverse direction. In order to cope with these properties, the anchoring devices can in principle be realized with structural steel cables, fibre ropes or tubular steel profiles (tethers) closely spaced along the tunnel length.

The most important advantages of the SFT structural concept over classical aerial bridges are (1) the fact that costs increase only linearly with the span length, (2) the reduced environmental impacts due to a smaller land footprint and (3) the ability to operate in all weather conditions. This last aspect is, nowadays, of particular concern due to the significant effects of climate change on the operability requirements of bridges and viaducts [9].

For all these reasons, there is a growing interest in the study of SFTs, as it is demonstrated, for example, by the recent publication of the first design guidelines by the International Federation for Structural Concrete [10].

Due to their slenderness and inherent flexibility, SFTs are very prone to the effect of dynamic loads such as traffic [11–17], seismic [3,18–31] and hydrodynamic loads.

Within this context, waves-induced forces are deemed to be the most critical for serviceability and fatigue life assessments of the whole SFT, because of their persistent and cyclic nature, as well as of their effect on the anchoring devices, which are vulnerable to hardly predictable fatigue phenomena [32,33].

Most of the studies of the literature about hydrodynamic loads deal with empirical and numerical models based either on the Morison equation or diffraction theory [33–43], which are formulated considering several limiting hypotheses about the fluid and under ideal waves and current conditions. On the contrary, realistic loading conditions are typically associated with a vast variety of complex phenomena (e.g. wave-current interaction), which usually require Computational Fluid Dynamics (CFD) tools to be solved in a reliable and quantitative way.

However, both numerical models and CFD simulations typically entail significant computational burden, making them unfeasible solutions for the conceptual design phase of SFTs.

Experimental tests on prototypes have also been carried out with reference to single SFT segments, short-span tube elements or small-scale two dimensional tests [35,44–49].

Nonetheless, they tend to be valid for the specific case only, limiting the generalizations of the achieved results due to the inability to simultaneously satisfy all the similitudes involved in the physics of both the fluid and the structure [50,51].

Despite the level of approximation it involves, Morison's approach [52] has been widely adopted in the literature to address the hydrodynamic response of SFTs at the structural level and it is considered sufficiently accurate for the purpose of the present work as well.

One of the key features of seabed-anchored SFTs is that the anchoring elements typically provide most of the stiffness to the overall system (both along heave and sway directions), while nearly the totality of the mass of the structure is concentrated along the tube. As a consequence, global vibration modes of the SFT usually involve significant displacements of the tunnel and quasi-static displacements of the tethers. On the contrary, almost all local vibrations modes involve vibrations of the tethers. They result from direct hydrodynamic loading and significant dynamic displacements of the tethers. They are characterized by values of natural frequencies which are well-separated from those of the global vibration modes.

Moreover, due to the smallness of the tube dimensionless bending stiffness, lower order modes of the SFT are characterized by closely spaced natural frequencies and the corresponding mode shapes tend to localize in the most flexible portion of the structure [53].

In order to account for the specificities of the dynamic response of SFTs in an efficient manner, a novel dynamic substructuring technique has been presented in [54], and adopted in the same work to classify the motion regimes of the SFT subjected to wave loads. While the global hydrodynamic response of the system has been found to be quasi-static, the tethers may behave in a dynamic manner under both direct and indirect dynamic excitation. The indirect excitation is caused by the motion of the tunnel, which can potentially lead to simple or parametric resonance of the tethers [55].

Given the significance of these hydrodynamic loading conditions, ensuring the long-term safety and durability of SFTs is of utmost importance. This underscores the need for quick and reliable engineering solutions to be adopted from the early stages of the structure's conceptual design.

Therefore, the aim of the present work is to investigate the hydrodynamic response of the anchoring elements by means of an analytical approach, exploiting the aforementioned peculiarities of the SFTs dynamic behavior, in order to derive closed-form approximate expressions involving the parameters governing the dynamic response of the coupled SFT, i.e., the tunnel-plus-mooring system. On this respect, the possible dynamic interaction between a global vibration mode of the SFT and the local vibration mode involving the tether is addressed, without neglecting a priori the coupling between the tethers and the tube, by defining a reduced-order 2D cross-sectional model of the SFT.

Under the hypothesis of rigid section, the submerged tube is modeled with two degrees of freedom, namely the vertical (i.e. heave) and horizontal (i.e. sway) displacements, while its torsional behavior (i.e. roll) is disregarded. The stiffness and mass associated to these two degrees of freedom are defined to be representative of a global vibration mode of the SFT.

This choice is motivated by the fact that the cluster of low-order global vibration modes responds in a quasi-static manner to hydrodynamic loads. The response of the cross-section, hence, is characterized by the same frequency content of the load and its vibration amplitude is given by the superposition of the quasi-static modal contributions.

This amplitude depends on the position of the cross-section observed and on the shapes of the low-order global vibration modes; in the model herein presented the amplitude of vibration of the cross-section is, hence, treated as a free loading parameter, in order to keep the approach general.

As per the anchoring elements, a 2D reduced-order model is employed, which describes planar vibrations of the tethers about their static equilibrium configuration. Such model accounts for both geometrical nonlinearities and supports motion, and it is based on the decomposition of the tether displacements in quasi-static and dynamic components originally proposed in [56].

The paper is articulated as follows. Section 2 deals with the modeling of the hydrodynamic loads acting on the SFT. Section 3 addresses the local dynamics of the tethers, by developing a 2D reduced-order model of taut-inclined submerged tethers. Section 4 presents a 2D cross-sectional model of the SFT, fully accounting for the coupling between a global mode of the tube and the dynamics of the tethers. Within this framework, different significant loading scenarios are clearly identified. Section 5 applies the multiple timescales perturbation method to derive closed-form expressions of the tethers steady-state vibration amplitude, for each loading case previously derived. Section 6 validates the closed-form expressions against numerical solution of the coupled system of equations and presents extensive parametric analyses on the technically-relevant design parameters of the tethers. Finally, Section 7 draws the conclusions of the work.

2. Hydrodynamic load on the SFT

The hydrodynamic loading acting on the SFT is usually modeled starting from the spectral representation of elevation of the wind-induced waves for a certain return period.The Power Spectral Density (PSD) of the wave elevation in deep-water conditions can be expressed as (see e.g. [57,58]):

$$S_\eta(\omega) = C_0\omega^{-m}\ \exp(-B_0\,\omega^{-n}) \tag{1}$$

where the coefficients C_0, B_0, m and n allow to uniquely define the spectrum. In the most widespread case, m and n are respectively set equal to 5 and 4, while several empirical expressions for C_0 and B_0 have been proposed in the literature, based on experimental measurements.

For instance, according to Bretschneider [59]:

$$C_0 = 0.0081\,g^2 \qquad B_0 = 3.11/H_s^2 \tag{2}$$

where g is the gravity acceleration and H_s is the significant wave height, which is defined as the arithmetic average of the highest one-third of the waves in a wave record [57].

The PSD of the water kinematic quantities (i.e., velocity and acceleration of the water particles) are then related to the PSD of the wave elevation thanks to suitable transfer functions, which directly stems from the adopted wave kinematic theory (such as the linear Airy or the nonlinear Stokes wave theories [58]). Fig. 2 depicts the PSD of the wave elevation for two different significant wave heights (i.e. $H_s = 14$ m and $H_s = 5$ m), which are representative of two different wave return periods.

As it can be appreciated from Fig. 2, both PSDs are narrow-banded. The energy content of the load is spread over a very narrow region of circular frequencies, and the intensity of the input is rapidly decreasing moving away from the peak spectral ordinate. For this reason, in the extreme idealized case, the frequency content of the loading can be modeled as a pure mono-harmonic function. This simplification will be adopted later on in this work to describe the loading acting on the SFT, within an analytical deterministic framework (see Section 4.5).

It is worth noting that, although harmonic functions do not reproduce the stochastic nature of realistic ocean-wave loading, they correspond to a regular-wave representation that is routinely employed in the design and verification of moored floating structures and submerged systems within offshore engineering practice [58].

The hydrodynamic force acting on the SFT can be then expressed according to the classical Morison formulation, which can be considered as an empirical approach to compute wave-induced forces on slender cylindrical structural elements, whenever the wavelength of the incident wave is large enough compared to the characteristic dimension of the structure. This amounts to declare that diffraction effects are negligible. This hypothesis is always verified for the case of the tethers, given their relatively small diameter.

For what concerns the tube cross-section, however, it may not be the case for waves having larger probability of occurrence (i.e., having lower significant height). Nonetheless, given the lower excitation intensity, and the inertia-dominated regime, Morison's approach may be considered adequate on the structural grounds also for the case of the tube (see, e.g. [34,39,60]).

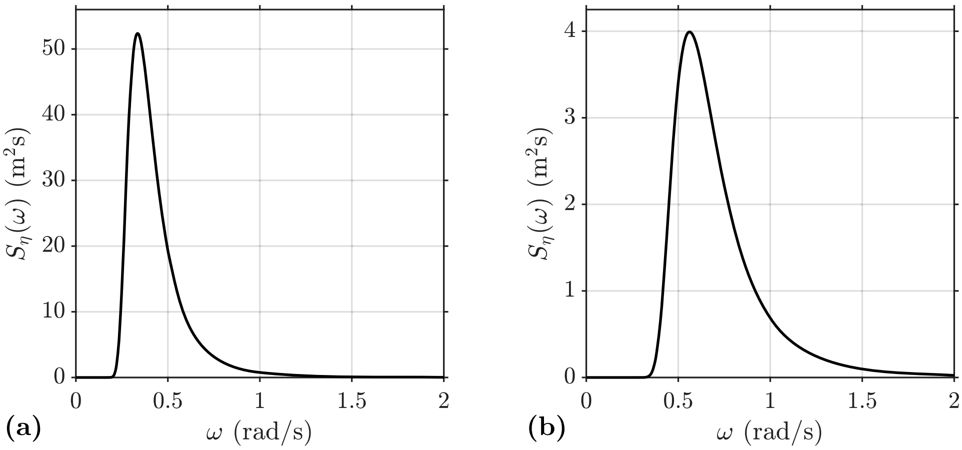

Fig. 2. Bretschneider wave elevation spectrum $S_\eta(\omega)$ for H_s = 14 m (a) and for H_s = 5 m (b).

Let us first tackle the hydrodynamic force per unit of length acting on the tube cross-section. Superimposing the effect of both inertia and drag forces, the Morison force per unit of length reads [52]:

$$q_T(x_T,t) = C_{D,T}\,\rho_w \frac{D_T}{2}\,|u(x_T,t;y^*) + U(x_T;y^*)|\Big(u(x_T,t;y^*) + U(x_T;y^*)\Big) + C_{I,T}\,\rho_w \pi \frac{D_T^2}{4}\,\dot{u}(x_T,t;y^*) \tag{3}$$

where $C_{I,T}$, $C_{D,T}$ and D_T denote, respectively, the inertia coefficient, drag coefficient and external diameter of the tube cross-section, while ρ_w is the water density.

Moreover, $x_T \in [0, L_T]$ is an abscissa spanning the total length of the SFT (L_T), while u, $\dot{u}$ and U denote, respectively, the water particle velocity and acceleration, and the steady current velocity evaluated at a depth corresponding to the tube's centroid depth (i.e. $y = y^*$).

In Eq. (3), the effect of the structural velocity of the tube has been disregarded because it is considered to be negligible compared to the fluid velocity.

By considering now a generic anchoring element, the Morison force per unit of length acting on a representative inclined cylindrical tether may be expressed as [58]:

$$q(x,t) = C_D\,\rho_w \frac{D_o}{2}\,|u_\perp(x,t) + U_\perp(x) - \dot{w}(x,t)|\big(u_\perp(x,t) + U_\perp(x) - \dot{w}(x,t)\big) + C_I\,\rho_w \pi \frac{D_o^2}{4}\,\dot{u}_\perp(x,t) \tag{4}$$

where $u_\perp$, $\dot{u}_\perp$ and $U_\perp$ denote respectively, the water particle velocity, water particle acceleration and the steady current velocity normal to the chord of the tether. Moreover, C_D, C_I and D_o denote, respectively the drag coefficient, inertia coefficient and external diameter of the tether cross-section, while $x \in [0, L_0]$ is an abscissa spanning the inclined chord length of the generic tether (L_0), highlighting the space dependence of the load along the element's development length.

It is worth noting that in this case it is crucial to explicitly account for the structural velocity of the system (i.e. $\dot{w}(x,t)$), since it is deemed to be relevant for the fluid-structure coupled interaction, because of the inherent slenderness of the tether. Finally, it is important to highlight that the added-mass contribution given by the fluid surrounding the tethers will be taken into account later on in this work by defining a virtual mass per unit of length (see Eq. (12)), but could in principle be incorporated in Eq. (4), as an inertially-driven contribution in the structural acceleration.

In order to better characterize the loading conditions on the SFT, it is also convenient to introduce the so-called Keulegan-Carpenter number (Kc). The latter is a useful non-dimensional number which measures the relative importance of the drag force compared to the inertia force for bluff bodies subject to an oscillatory fluid flow. This can be expressed as:

$$\mathrm{Kc} = \frac{u_0\,T}{D} \tag{5}$$

where D is a characteristic dimension of the structure (in this case it can be regarded as the external diameter of the considered structure, either the tube (D_T) or the tethers (D_o)), T is the period of oscillations of the fluid, while u_0 is the maximum value of the normal component of the water particle velocity (see e.g. [58]). Inspection of Eq. (5) for typical values of wave periods and water particle velocities reveals that the forcing is inertially dominated for the tube cross-section (i.e. Kc < 1), while for the anchoring elements the drag term is comparatively more important (Kc $\gg$1).

For this reason, in the present work the hydrodynamic load on the tube is taken to be purely inertial, whereas the drag force is treated as the sole direct load acting on the tethers.

This modeling assumption is routinely adopted in offshore engineering practice, e.g., for jacket platforms and floating offshore wind turbines, in which the primary fixed or floating body has relatively large characteristic dimensions, while the bracings or mooring lines/tethers are slender and flexible [61].

Furthermore, both the shape and magnitude of the current profile ($U(y)$) are strongly site-dependent. To avoid potential biases associated with a specific modeling choice, steady current is neglected in the present work. This simplification leads to an underestimation of the equivalent damping of the system while simultaneously reducing the magnitude of the external forcing through the modification of the relative fluid–structure velocity.

A more refined assessment of the role of steady current could be pursued by applying a statistical cubicization of the drag force acting on the tethers (see Eq. (4)), as proposed in [62,63]. This approach has been followed in [60], in conjunction with a Volterra series expansion (see, e.g. [64,65]) to develop a single-degree-of-freedom model of the fixed-supports tether that accounts for both geometrical and load-induced nonlinearities in closed form.

For the purposes of the present work, however, an equivalent linearization of the drag force is adopted and deemed sufficient within the conceptual framework herein developed. This choice is further justified by the fact that the forcing amplitude is retained as a free parameter, and the system response is investigated through systematic parametric analyses (see Section 6.2).

According to the simplifications introduced above, Eqs. (3) and (4) respectively translate to:

$$q_T(x_T,t) = C_{I,T}\rho_w \pi \frac{D_T^2}{4}\dot{u}(x_T,y^*,t) \tag{6}$$

and:

$$q(x,t) = C_D \rho_w \frac{D_o}{2}\left|u_\perp(x,t) - \dot{w}(x,t)\right|\left(u_\perp(x,t) - \dot{w}(x,t)\right) \tag{7}$$

3. Local dynamics of the anchoring elements

3.1. Preliminaries

Let us make reference to Fig. 3 and consider a generic tether inclined with an angle θ over the horizontal line, having initial chord length L_0, external diameter D_o, mass per unit of length γ_s, axial stiffness EA_0 and subject to a static tension $T_0 > 0$ (i.e., a pretension). The self-weight per unit of length of the cable is denoted by w_s (i.e. $w_s = \gamma_s g$,), while the symbol br indicates its buoyancy ratio, namely the ratio of the hydrostatic forces per unit of length and the self-weight per unit of length.

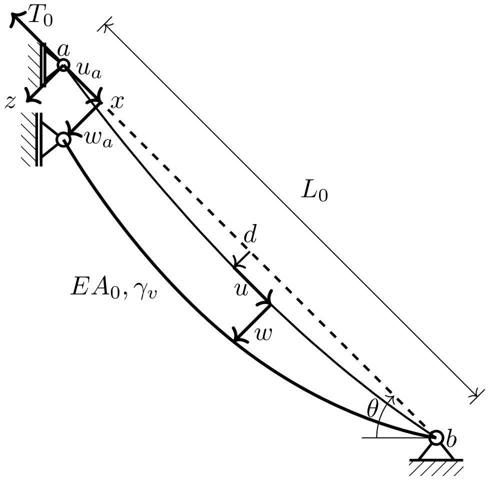

Fig. 3. Structural scheme of a perfectly flexible sagged cable subject to an arbitrary motion of support a.

The buoyancy ratio of a water-immersed circular hollow cross-section tether can be computed as:

$$\mathrm{br} = \frac{\rho_w D_o^2}{4\rho_s t_o (D_o - t_o)} \tag{8}$$

where t_o is the thickness of the hollow profile, whereas ρ_s and ρ_w indicate the material density of the steel and water, respectively. Eq. (8) evaluates the buoyancy ratio assuming a uniform circular hollow cross-section along the full tether length, thereby neglecting the additional displaced water volume introduced by end connections of the tether in real applications.

Furthermore, let us denote by λ^2 the elasto-geometric Irvine's parameter [66]:

$$\lambda^2 = \Gamma^2 \cos^2(\theta)\,\frac{1}{\varepsilon_0} \tag{9}$$

which accounts for the relative importance between elastic and geometric stiffness effects, within the small-sag cable theory. In Eq. (9) $\Gamma = w_s(1-\mathrm{br})L_0/T_0$ has been introduced in compact form, while ε_0 is the initial static axial strain of the cable. It is now convenient to introduce the static engineering strain ε_0 as a function of the non-dimensional pretension $\eta_0 = T_0/T_y$:

$$\varepsilon_0 = \frac{T_0}{EA_0} = \frac{\eta_0 T_y}{EA_0} = \frac{\eta_0 f_y}{E} \tag{10}$$

where $T_y = f_y A_0$ is the yielding tensile force and f_y is the yielding stress of the material.

The non-dimensional pretension is directly proportional to the BWR of the SFT (i.e., $\eta_0 \propto$ BWR). The static stress which acts on the generic tether can be then conveniently expressed as a fraction of the yielding stress, i.e.: $\sigma_s = T_0/A_0 = \eta_0 f_y$.

The midspan sag d of the inclined tether can be computed, according to the classic parabolic approximation as:

$$d = \frac{w\, L_0^2}{8\, T_0}\cos\theta = \frac{w_s(1-br)\, L_0^2}{8\, T_0}\cos\theta \tag{11}$$

Moreover, the mass per unit of length which should be considered for the natural frequencies computation is the so-called "virtual" mass per unit of length:

$$\gamma_v = \gamma_s + C_A\, \gamma_w \tag{12}$$

The latter takes into account the presence of the fluid around the tether that acts as an added mass when dealing with its dynamic response. This portion of the fluid surrounding the section is, indeed, assumed to share the same motion of the tether. The added-mass coefficient C_A depends on the cross-section of the tether and, in the case of a circular cross-section, $C_A = 1$ is usually adopted (see e.g., [57,58]).

3.2. Motion decomposition

Leveraging their relatively small bending stiffness, the tethers of the SFT are modeled as perfectly flexible structural elements, according to a reduced-order cable model (ROM) firstly presented by Warnitchai et al. in [56]. Formal differences of the present ROM for the case of SFT anchoring elements compared to that proposed in [56], are given by (i) the fact that they are immersed in water and (ii) that the hypothesis related to the small magnitude of the quasi-static axial stress σ_q with respect to the static stress σ_s (i.e., $\sigma_q \ll \sigma_s$), enforced in [56], has been here removed.

Let us consider the reference system depicted in Fig. 3, in which the x axis spans the whole chord length, i.e. $0 < x < L_0$, and the dynamic tether motion along x and z directions is denoted by u and w, respectively.

Since the focus of the work is related to the hydrodynamic loads, the bottom support of the tether (point b) is kept fixed, while a generic form of support motion at point a is considered, which is supposed to model the coupling with the main tube.

To do so, let us express the displacements along the directions u and w at supports a and b according to the following equations:

$$u(x=0,t) = u_a(t) \qquad w(x=0,t) = w_a(t) \tag{13a}$$

$$u(x=L_0,t) = 0 \qquad w(x=L_0,t) = 0 \tag{13b}$$

From now on, the time dependence of the support motion will be implicitly assumed, so that these quantities will be indicated only with the symbols u_a and w_a. The support motion is considered to be small if compared to the initial length of the tether. The following physically sound hypotheses are introduced (as in [56]):

$$|u_a|, |w_a| \ll L_0 \tag{14}$$

Hence,

$$\left(\frac{u_a}{L_0}\right)^2, \left(\frac{w_a}{L_0}\right)^2 \ll \frac{|u_a|}{L_0} \tag{15}$$

The main hypothesis of the model is that the total time-dependent displacements of the tether can be decomposed into the sum of two parts: the quasi-static component (denoted by the superscript q) and modal component (denoted by superscript m). The former are the displacements of the tether which moves as an elastic tendon due to the support motion, while the latter are expressed as a combination of the linear undamped modes of a cable with fixed ends. It is possible to write:

$$u(x,t) = u^q(x,t) + u^m(x,t) \tag{16a}$$

$$w(x,t) = w^q(x,t) + w^m(x,t) \tag{16b}$$

The quasi-static part of the displacements can be computed according to the following equations (cf. [56]):

$$u^q(x,t) = u_a\left(1 - \frac{E_q}{E}\frac{x}{L_0}\right) - \frac{\lambda^2}{4}\frac{E_q}{E}u_a\left[\frac{x}{L_0} - 2\left(\frac{x}{L_0}\right)^2 + \frac{4}{3}\left(\frac{x}{L_0}\right)^3\right] \tag{17a}$$

$$w^q(x,t) = w_a\left(1 - \frac{x}{L_0}\right) + \frac{1}{2}\frac{\iota L_0 E_q}{\sigma_s^2}u_a\left[\frac{x}{L_0} - \left(\frac{x}{L_0}\right)^2\right] \tag{17b}$$

In the previous equations, the so-called Dischinger-Ernst E-modulus has been conveniently introduced:

$$E_q = \frac{E}{1 + \lambda^2/12} \tag{18}$$

as well as the following quantity ι:

$$\iota = \frac{w_s(1-\mathrm{br})\cos\theta}{A_0} \tag{19}$$

which physically represents the component of the weight per unit of volume directed along the normal to the chord of the tether.

For what concerns the modal motions, the separation of variable is employed, whereas the axial modal motion is assumed to be negligible compared to the transverse one, since it involves frequencies much higher than those associated with the in-plane transverse vibrations.

$$|u^m(x,t)| \ll |w^m(x,t)| \tag{20}$$

$$w^m(x,t) = \psi(x)\, z(t) \tag{21}$$

Eq. (21) can be regarded as a special form of a Rayleigh-Ritz discretization procedure, in which only one shape function $\psi(x)$ has been retained. The latter is selected as the first eigenfunction of the taut-string with fixed ends:

$$\psi(x) = \sin(\pi x/L_0) \tag{22}$$

Additionally, the temporal coefficient $z(t)$ can be interpreted as the generalized modal coordinate of the in-plane motion for the considered tether.

The expression of the dynamic strain reads:

$$\varepsilon_d(t) = -\frac{E_q}{E}\frac{u_a}{L_0} + \frac{\iota}{\sigma_s}c_1 z(t) + \frac{\iota E_q}{\sigma_s^2}\frac{u_a}{L_0}c_1 z + c_2 z^2(t) \tag{23}$$

where coefficients $c_1 = 2/\pi$ and $c_2 = \pi^2/(4L_0^2)$ are results of simple integrals of trigonometric functions.

The dynamic stress is linearly related to the dynamic strain:

$$\sigma_d(x,t) = E\varepsilon_d(x,t) \tag{24}$$

Warnitchai et al. included in the definition of σ_d the quasi-static contribution to the axial stress, which takes the physical meaning of the stress associated to the quasi-static motion of the anchoring element. This contribution is called quasi-static stress (σ_q) and can be obtained from direct linearization of Eq. (24). Its expression simply reads:

$$\sigma_q(t) = -E_q\frac{u_a(t)}{L_0} \tag{25}$$

In their original work, this term has been neglected since for typical wind-engineering applications (e.g. for stay cables) it is deemed to be small compared to the magnitude of the static stress σ_s (i.e., $\sigma_q \ll \sigma_s$). On the contrary, as already shown in [30], this hypothesis ceases to be valid for typical situations involving submerged tethers. For this reason, such contribution has been accounted for in the present work.

3.3. Equation of motion

Based on a classical Lagrangian formulation, the equation of motion of the generic tether is derived:

$$m\left(\ddot{z} + 2\xi\omega\dot{z} + \omega^2 z\right) + \nu z^3 + 3\beta z^2 + 3\tilde{\beta}z^2 u_a - 2(\eta-\mu)u_a z + \zeta\ddot{w}_a + \alpha\ddot{u}_a = F \tag{26}$$

where the modal generalized force can be expressed as:

$$F = \int_0^{L_0} Z A_0 \psi(x) dx \tag{27}$$

Z being a volume force which acts in the in-plane direction, ξ the viscous damping coefficient of the tether, m its virtual modal mass (see Eq. (A.1)) and ω its natural circular frequency (see Eq. (A.2)). All the coefficients appearing in Eq. (26) are reported into App. A. Such coefficients are slightly different compared to those presented in [56], because the hypothesis related to the small magnitude of the quasi-static axial stress σ_q with respect to the static stress σ_s (i.e., $\sigma_q \ll \sigma_s$) has been removed in the present work.

The equation for the in-plane vibrations of the tether presents both quadratic ($3\beta z^2$) and cubic (νz^3) geometrical nonlinear terms, as well as a Mathieu-like term ($2(\eta-\mu)u_a z$), and a mixed term, which involves both quadratic nonlinearities and support motion ($3\tilde{\beta} z^2 u_a$). Inertially-driven contributions are also present, which stem from having accounted for the supports motion, namely $\zeta\ddot{w}_a$ and $\alpha\ddot{u}_a$.

3.4. Non-dimensional formulation

By introducing a set of suitable characteristic quantities, it is possible to write the dimensionless version of the equation of motion. Let us denote with L_c a characteristic displacement of the system and with ω_c a characteristic circular frequency, which are respectively selected as the maximum value of the midspan sag achieved for an equivalent horizontal tether (i.e., having the two supports at the same level) and as the first wet in-plane natural circular frequency of the taut-string model:

$$L_c = \frac{w_s(1-\mathrm{br})\,L_0^2}{8\,T_0} = \frac{\Gamma L_0}{8} \tag{28}$$

$$\omega_c = \frac{\pi}{L_0}\sqrt{\frac{T_0}{\gamma_v}} \tag{29}$$

It is worth noticing that the characteristic displacement L_c is not an observed quantity of the system under consideration. It is different from the real sag of the tether (see Eq. (11)). This choice is necessary to the avoid a singularity for vertical anchoring elements, having zero sag. The dimensionless time variable is then defined as $\tau = \omega_c t$. By introducing the non-dimensional modal coordinate ($\bar{z} = z/L_c$) and support displacements ($\bar{u}_i = u_i/L_c$ and $\bar{w}_i = w_i/L_c$, $i = a, b$), the following non-dimensional equation of motion is readily obtained:

$$\ddot{\bar{z}} + 2\xi\bar{\omega}\dot{\bar{z}} + \bar{\omega}^2\bar{z} + \bar{\nu}\bar{z}^3 + 3\bar{\beta}\bar{z}^2 - 3\tilde{\bar{\beta}}\bar{z}^2\bar{u}_a - 2(\bar{\eta} - \bar{\mu})\bar{u}_a\bar{z} + \zeta\ddot{\bar{w}}_a + \bar{\alpha}\ddot{\bar{u}}_a = \bar{F}(\tau) \tag{30}$$

All the dimensionless coefficients appearing in the previous equations are reported in App. B.

3.5. Linearization of the hydrodynamic load

In order to proceed with the next developments, a proper linearization of the drag force acting on the tethers (Eq. (7)) is necessary. This force per unit of length $q(x,t)$ can be regarded as the equivalent of the product ZA_0 which appears in the definition of the modal generalized external load (see Eq. (27)) and is herein modeled according to the classical Morison approach, following the developments reported in Section 2.

The key hypothesis which is needed to linearize Eq. (7) in a deterministic setting is that the drag force caused by a wave on an oscillating cylinder can be approximated as the superposition of a force caused by a wave on a stationary cylinder and a force exerted on an oscillating cylinder in still water. By neglecting the quasi-static velocity contribution, the drag force per unit of length can be, hence, expressed as:

$$q(x,t) \simeq C_D\rho_w\frac{D_o}{2}|u_\perp(x,t)|u_\perp(x,t) - C_D\rho_w\frac{D_o}{2}|\dot{w}(x,t)|\dot{w}(x,t) \tag{31}$$

and the associated fixed-supports dimensionless forced equation of motion of the tether reads:

$$\ddot{\bar{z}}(\tau) + 2\xi^s\bar{\omega}\dot{\bar{z}}(\tau) + \bar{\omega}^2\bar{z}(\tau) + 3\bar{\beta}\bar{z}^2(\tau) + \bar{\nu}\bar{z}^3(\tau) = \frac{2L_0}{\pi^2 T_0 L_c}\int_0^{L_0} q(x,t)\,\psi(x)dx \tag{32}$$

which is found after substitution of $\bar{u}_a = \bar{w}_a = 0$ in Eq. (30).

In order to linearize both terms of Eq. (31) according to a deterministic technique, the wave particle velocity is expressed as a harmonic function, resonant with the natural circular frequency of the tether (i.e. $\bar{u}_\perp = \bar{b}\sin(\bar{\omega}\tau)$), and a harmonic steady-state solution of the equation of motion with fixed supports is sought as well (i.e. $\bar{z} = \bar{a}\cos(\bar{\omega}\tau + \Phi)$). For the sake of readability, the complete derivation of the linearized expression is fully detailed in App. C.

Expressing the forcing term in the fluid velocity according to a classical Fourier series representation, the following result is obtained:

$$\bar{\Upsilon}_1\bar{b}^2\,\sin(\bar{\omega}\tau)|\sin(\bar{\omega}\tau)| = \frac{8\bar{b}^2\bar{\Upsilon}_1}{3\pi}\sin(\bar{\omega}\tau) = \tilde{\bar{f}}\sin(\bar{\omega}\tau) \tag{33}$$

$\bar{\Upsilon}_1$ being a constant given by Eq. (C.10) and $\tilde{\bar{f}}$ a dimensionless force amplitude, which reads:

$$\tilde{\bar{f}} = \frac{16}{3\pi^2}\frac{C_D\rho_w D_o L_c}{\gamma_v}\bar{b}^2 \tag{34}$$

The previous expression will be useful for the next developments, and in particular whenever direct loading conditions acting on the anchoring element will be addressed (see Section 5.2.3).

In App. C the Harmonic Balance Method (HBM) is also used to determine the expression of an equivalent viscous modal damping ratio, which represents the effect of the nonlinear feedback term in the structural velocity (i.e. the second term of Eq. (31)). After simple algebra, the total modal viscous damping ratio of the tether is found to be:

$$\xi(\bar{a}) = \xi^s + \xi^{eq}(\bar{a}) = \xi^s + \bar{K}_d\,\bar{a} \tag{35}$$

where ξ^s is the structural modal damping ratio, $\bar{a}$ is the non-dimensional steady state amplitude of vibration, and $\bar{K}_d$ is a non-dimensional "equivalent damping" coefficient given by the following equation:

$$\bar{K}_d = \frac{16}{9\pi^2}\frac{C_D\,\rho_w\,D_o\,L_c}{\gamma_v} \tag{36}$$

It is worth noting that this additional damping contribution stems from the effect of an external force exerted on an oscillating cylinder in still water. As a consequence, it should be considered not only in the case of direct excitation of the tether, but also when indirect excitation caused by the tunnel is considered. Therefore, Eq. (35) will be systematically adopted in the following developments for the solution of the tether equation of motion, within a perturbation approach, to account for the effects of the added-damping due to fluid-structure interaction (see Section 5). The linearized non-dimensional equation of motion of the fixed-supports tether, externally forced, finally becomes (cf. Eq. (32)):

$$\ddot{\bar{z}}(\tau) + 2(\xi^s + \xi^{eq})\bar{\omega}\dot{\bar{z}}(\tau) + \bar{\omega}^2\bar{z}(\tau) + 3\bar{\beta}\bar{z}^2(\tau) + \bar{\nu}\bar{z}^3(\tau) = \tilde{\bar{f}}\,\sin[\bar{\omega}(1+\Delta)\,\tau] \tag{37}$$

where Δ is a small detuning parameter (see Sections 4.5 and 5).

Finally, it is worth noting that this approximation preserves the leading-order forcing term and the associated energy dissipation in the vicinity of the primary resonance. However, by construction, the equivalent linear model suppresses the generation of higher harmonics to the effective forcing and damping that would arise from the fully nonlinear drag term [61].

As a consequence, the perturbation solutions should be interpreted as capturing the dominant, near-resonant response features, while potentially underestimating response asymmetries and other weakly nonlinear effects away from the resonance region. This limitation is, however, consistent with the introduction of the small detuning parameter, which is specifically intended to represent the nearly-resonant dynamic response of the tether, in the spirit of classical perturbation approaches [67].

4. Cross-sectional model of the SFT

Disregarding torsional rotations, the cross-section of the tube is modeled as a rigid body, characterized by two degrees of freedom, namely the heave and sway displacements, which are respectively denoted by the symbols $w_T(t)$ and $v_T(t)$. The mass (m_T) of the body, the stiffnesses ($k_{T,h}$ and $k_{T,v}$) and the damping coefficients ($c_{T,h}$ and $c_{T,v}$) associated to the sway and heave degrees of freedom, respectively, are selected to be representative of a global vibration mode of the SFT (see Fig. 4).

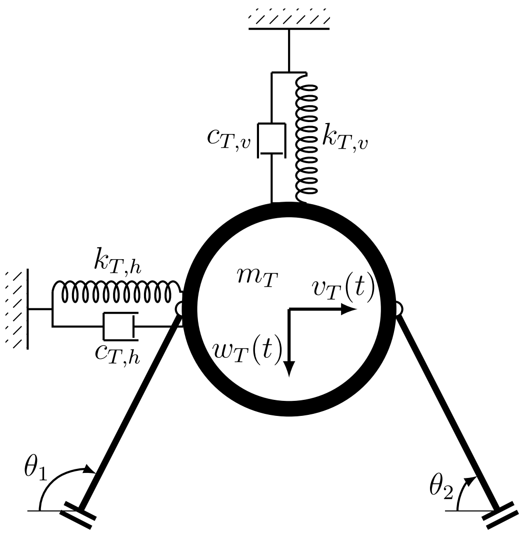

Fig. 4. Model of the rigid cross-section of the tunnel as an equivalent two-dofs oscillator.

The original mooring configuration, consisting of four symmetric tethers (see Fig. 1(b)), is here simplified by neglecting the small variation in the inclination angles θ between the inner and outer pairs of tethers, yielding two equivalent anchoring elements, as depicted in Fig. 4.

Each tether is modeled according to the small-sag cable theory through the reduced-order model presented in Section 3.

The vibrations of the moored SFT cross-section are studied about the static equilibrium configuration, established under the combined effect of the tube BWR, which induces a static pretension in the tethers, and the buoyancy ratio of the tethers themselves (br). Additionally, the time-varying tilt angles between the direction tangent to the deformed tether configuration at the top support and its chord are neglected.

Under these assumptions, the interface forces exchanged between the tube and the tethers reduce to the projection of the time-varying dynamic tension T of each tether onto both heave and sway directions (see Fig. 5).

4.1. System interactions

To explicitly derive the coupled equations of motion, compatibility conditions between each tether ($j = 1, 2$) and the rigid cross-section of the tunnel must be established. By introducing the following non-dimensional displacements:

$$\bar{w}_T = \frac{w_T}{L_c} \qquad \bar{v}_T = \frac{v_T}{L_c} \tag{38}$$

one simply has:

$$\bar{u}_{a_j}(\tau) = \bar{v}_T(\tau)\cos\theta_j + \bar{w}_T(\tau)\sin\theta_j \qquad \bar{w}_{a_j}(\tau) = -\bar{v}_T(\tau)\sin\theta_j + \bar{w}_T(\tau)\cos\theta_j \tag{39}$$

By differentiating Eq. (39) one or two times with respect to the dimensionless time variable, the following expressions are straightforwardly obtained:

$$\dot{\bar{u}}_{a_j}(\tau) = \dot{\bar{v}}_T(\tau)\cos\theta_j + \dot{\bar{w}}_T(\tau)\sin\theta_j \qquad \dot{\bar{w}}_{a_j}(\tau) = -\dot{\bar{v}}_T(\tau)\sin\theta_j + \dot{\bar{w}}_T(\tau)\cos\theta_j \tag{40}$$

$$\ddot{\bar{u}}_{a_j}(\tau) = \ddot{\bar{v}}_T(\tau)\cos\theta_j + \ddot{\bar{w}}_T(\tau)\sin\theta_j \qquad \ddot{\bar{w}}_{a_j}(\tau) = -\ddot{\bar{v}}_T(\tau)\sin\theta_j + \ddot{\bar{w}}_T(\tau)\cos\theta_j \tag{41}$$

At this stage, recalling the expression of the dynamic axial strain (see Eq. (23)), the non-dimensional dynamic tension acting on the jth tether, can be expressed as:

$$\bar{T}_j(\tau) = \frac{EA_0\varepsilon_{d,j}(\tau)}{\omega_c^2 L_c m_T} \qquad j = 1, 2 \tag{42}$$

where m_T denotes the wet mass of the rigid body, i.e. the modal mass of the selected vibration mode of the SFT. Projection of this force for both anchoring elements, along the vertical and horizontal directions (i.e. along w_T and v_T) leads to (cf. Fig. 5):

$$\bar{V}(\tau) = \bar{T}_1(\tau)\sin\theta_1 + \bar{T}_2(\tau)\sin\theta_2 \qquad \bar{H}(\tau) = \bar{T}_1(\tau)\cos\theta_1 + \bar{T}_2(\tau)\cos\theta_2 \tag{43}$$

These are the non-dimensional vertical and horizontal forces exchanged between the two subsystems, namely the tunnel and the tethers.

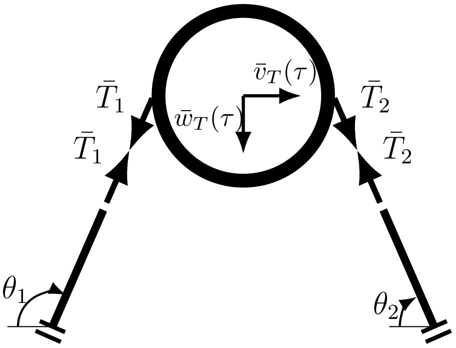

Fig. 5. Schematic of the interaction forces exchanged by the rigid body modeling the cross-section of the SFT and the equivalent tethers.

4.2. System of equations

Considering both vertical and horizontal dynamic equilibrium of the rigid body, along with Eq. (43), the following system of four dimensionless, coupled, second-order, ordinary nonlinear differential equations is obtained:

$$\begin{cases} \ddot{\bar{w}}_T + 2\xi_{T,v}\,\bar{\omega}_{T,v}\,\dot{\bar{w}}_T + \bar{\omega}_{T,v}^2\,\bar{w}_T = \bar{F}_{T,v}(\tau) + \bar{V}(\tau) \\ \ddot{\bar{v}}_T + 2\xi_{T,h}\,\bar{\omega}_{T,h}\,\dot{\bar{v}}_T + \bar{\omega}_{T,h}^2\,\bar{v}_T = \bar{F}_{T,h}(\tau) + \bar{H}(\tau) \\ \ddot{\bar{z}}_j + 2\xi\bar{\omega}\,\dot{\bar{z}}_j + \omega^2\,\bar{z}_j + \nu\,\bar{z}_j^3 + 3\bar{\beta}_j\,\bar{z}_j^2 + 3\bar{\tilde{\beta}}_j\,\bar{z}_j^2\left(\bar{v}_T\cos\theta_j + \bar{w}_T\sin\theta_j\right) + \\ -2(\bar{\eta} - \bar{\mu})\left(\bar{v}_T\cos\theta_j + \bar{w}_T\sin\theta_j\right)\bar{z}_j + \bar{\alpha}_j\left(\ddot{\bar{v}}_T\cos\theta_j + \ddot{\bar{w}}_T\sin\theta_j\right) + \\ +\zeta\left[\ddot{\bar{w}}_T\cos\theta_j - \ddot{\bar{v}}_T\sin\theta_j\right] = \bar{F}_j(t) \quad j = 1, 2 \end{cases} \tag{44}$$

where:

$$\bar{\omega}_{T,v} = \frac{1}{\omega_c}\sqrt{\frac{k_{T,v}}{m_T}} \qquad \bar{\omega}_{T,h} = \frac{1}{\omega_c}\sqrt{\frac{k_{T,h}}{m_T}} \tag{45}$$

and:

$$\xi_{T,v} = \frac{c_{T,v}}{2m_T\,\omega_c\,\bar{\omega}_{T,v}} \qquad \xi_{T,h} = \frac{c_{T,h}}{2m_T\,\omega_c\,\bar{\omega}_{T,h}} \tag{46}$$

denote the wet dimensionless circular frequencies and damping ratios of the rigid section along the vertical and horizontal directions, respectively (see Fig. 4), while $\bar{F}_{T,v}$ and $\bar{F}_{T,h}$ respectively represent the non-dimensional generalized external force of the rigid section along the vertical and horizontal directions. The external forces are obtained by projection of the inertial hydrodynamic load (see Eq. (6)), modeled according to the developments presented in Section 2, on the selected mode shape. All the dimensionless coefficients appearing in the previous equations are reported in App. B.

Eq. (42) may be expressed, more conveniently as:

$$\bar{T}_j(\tau) = \bar{\kappa}_0\left(\cos\theta_j\bar{v}_T + \sin\theta_j\bar{w}_T\right) + \bar{\kappa}_1\,\cos\theta_j\bar{z}_j + \bar{\kappa}_2\,\bar{z}_j^2 + \bar{\kappa}_3\left(\cos^2\theta_j\bar{z}_j\bar{v}_T + \cos\theta_j\sin\theta_j\bar{z}_j\bar{w}_T\right) \tag{47}$$

where the following non-dimensional coefficients have been introduced:

$$\bar{\kappa}_0 = -\frac{E_q A_0}{\omega_c^2 m_T L_0} \qquad \bar{\kappa}_1 = \frac{2EA_0 w_s(1-\mathrm{br})}{\omega_c^2\pi T_0 m_T} \qquad \bar{\kappa}_2 = \frac{\pi^2 EA_0 L_c}{4\omega_c^2 m_T L_0^2} \qquad \bar{\kappa}_3 = \frac{2EE_q A_0^2 L_c w_s(1-\mathrm{br})}{\omega_c^2 m_T \pi L_0 T_0^2} \tag{48}$$

Numerical inspection of the previous coefficients performed with reference to hollow circular cross-section tethers reveals that $\bar{\kappa}_1$, $\bar{\kappa}_2$ and $\bar{\kappa}_3$ are negligible compared to $\bar{\kappa}_0$, i.e. $\bar{\kappa}_i \ll \bar{\kappa}_0$ (for $i = 1, 2, 3$). This fact reflects in a modification of the sole static stiffness of the tunnel as a consequence of the coupling with the tethers. This allows to state that the dynamic coupling between the tube and the mooring system can be considered as a one-way coupling, i.e. the bare tunnel has a direct influence on the dynamic response of the mooring system and not vice-versa. As a consequence, a generic mooring cross-section of the tube is not influenced by the behavior of different mooring cross-sections close to the former one. Additionally, the heave (i.e., in-plane) and sway (i.e., out-of-plane) behavior of the SFT are practically decoupled.

Therefore, in the following sections, two simplified models are developed, which treat separately the heave (Section 4.3) and sway (Section 4.4) motion of the SFT.

As long as the drag force acting on the tube can be considered as negligible, this simplification is very accurate and allows to attack the two problems separately thanks to powerful analytical tools.

4.3. Heave motion of the SFT

Whenever the in-plane motion of the tunnel is concerned, the system can be regarded as symmetric. Therefore, the Eq. (44) simplify to a system of two ordinary differential equations that describe the interaction between the tunnel, treated as a single-dof rigid body characterized solely by its vertical displacement w_T, and an equivalent single tether, characterized by an inclination angle θ, and described by its modal coordinate $\bar{z}$:

$$\begin{cases} \ddot{\bar{w}}_T + 2\xi_{T,v}\,\bar{\omega}_{T,v}\,\dot{\bar{w}}_T + \bar{\omega}^2_{T,v}\,\bar{w}_T = \bar{F}_{T,v}(\tau) + \bar{c}_0\bar{w}_T \\ \ddot{\bar{z}} + 2\xi\bar{\omega}\,\dot{\bar{z}} + \bar{\omega}^2\,\bar{z} + \bar{v}\,\bar{z}^3 + 3\bar{\beta}\,\bar{z}^2 + 3\bar{\tilde{\beta}}\,\bar{z}^2\bar{w}_T\sin\theta - 2(\bar{\eta}-\bar{\mu})\bar{w}_T\sin\theta\,\bar{z} + \bar{\alpha}\ddot{\bar{w}}_T\sin\theta + \bar{\zeta}\,\ddot{\bar{w}}_T\cos\theta = \bar{F}(\tau) \end{cases} \tag{49}$$

with the definition:

$$\bar{c}_0 = \bar{\kappa}_0\,\sin^2\theta \tag{50}$$

4.4. Sway motion of the SFT

Whenever the out-of plane motion of the tunnel is concerned, the response of the system during its transient phase is non-symmetric. Therefore, it is necessary to describe separately the dynamics of the two tethers. However, the tunnel can still be treated as single-dof rigid body, described by the horizontal displacement ($\bar{v}_T$) only. The Eq. (44), hence, simplify to a system of three ordinary differential equations:

$$\begin{cases} \ddot{\bar{v}}_T + 2\xi_{T,h}\,\bar{\omega}_{T,h}\,\dot{\bar{v}}_T + \bar{\omega}^2_{T,h}\,\bar{v}_T = \bar{F}_{T,h}(\tau) + \sum_{j=1}^{2}\bar{c}_{0,j}\bar{v}_T \\ \ddot{\bar{z}}_j + 2\xi\bar{\omega}\,\dot{\bar{z}}_j + \omega^2\,\bar{z}_j + v\,\bar{z}_j^3 + 3\bar{\beta}_j\,\bar{z}_j^2 + 3\bar{\tilde{\beta}}_j\,\bar{z}_j^2\,\bar{v}_T\cos\theta_j - 2(\bar{\eta}-\bar{\mu})\,\bar{v}_T\cos\theta_j\bar{z}_j + \bar{\alpha}_j\,\ddot{\bar{v}}_T\cos\theta_j - \zeta\,\ddot{\bar{v}}_T\sin\theta_j = \bar{F}_j(t) \quad j = 1,2 \end{cases} \tag{51}$$

with the definition:

$$\bar{c}_{0,j} = \bar{\kappa}_0\,\cos^2\theta_j \quad j = 1,2 \tag{52}$$

If the inclination angles of the two tethers are supplementary (as it is often the case) such coefficients degenerate to $\bar{c}_0^* = \bar{\kappa}_0\,\cos^2\theta$, simplifying further the system of equations.

4.5. Formalization of the loading conditions

In order to derive closed-form analytical expressions for the dynamic response of the coupled cross-sectional model of the SFT, harmonic loading conditions are imposed on the system, applied either to the tube or to the tethers depending on the excitation scenario under consideration.

Although purely harmonic forcing does not capture the stochastic nature of realistic ocean wave loading (see Section 2), it corresponds to a regular wave analysis and constitutes a well-established framework for characterizing the deterministic coupled dynamics of the system. This approach is widely adopted in both offshore engineering practice and nonlinear dynamics, where harmonic excitation serves as the canonical tool for identifying resonance conditions, frequency response characteristics, and the influence of nonlinear phenomena [68,69].

Based on the classification of the motion regimes highlighted in [54] and discussed in Section 1 of the present work, as well as on the peculiarities of the hydrodynamic loads emphasized in Section 2, three main loading scenarios have been identified:

1. LC1: Hydrodynamic forces acting on the tunnel, Quasi-Simple-Resonant with the tether (1:1). In this case, the loading on the tether is neglected, since the interest is focused on the indirect excitation arising from the coupling with the tunnel. The forcing acting on the tunnel may be expressed as a harmonic function which depends on a small detuning parameter Δ, so that the loading frequency is centered around the dimensionless circular frequency of the tether $\bar{\omega}$, i.e.:

$$\bar{F}_T(\tau) = \bar{f}\,\sin[\bar{\omega}(1+\Delta)\,\tau] \qquad \bar{F}(\tau) = 0 \tag{53}$$

This holds both for the in-plane and out-of-plane motions of the SFT. This loading case will be treated in Section 5.2.1.

2. LC2: Hydrodynamic forces acting on the tunnel, Quasi-Parametric-Resonant with the tether (2:1). Also in this case, the loading on the tether is neglected, since the interest is on the indirect excitation arising from the coupling with the tunnel. The forcing on the tunnel may be again expressed as a harmonic function which depends on a small detuning parameter Δ, so that the loading frequency is centered around the value corresponding to twice the dimensionless circular frequency of the tether $\bar{\omega}$, i.e.:
$$\bar{F}_T(\tau) = \bar{f}\, \sin[\bar{\omega}\,(2+\Delta)\,\tau] \qquad \bar{F}(\tau) = 0 \tag{54}$$
This holds both for the in-plane and out-of-plane motion of the SFT. This loading case will be treated in Section 5.2.2.
3. LC3: Hydrodynamic forces acting on the tether, Quasi-Resonant (1:1) with the tether itself. The loading on the tunnel is neglected. The forcing on the tether can be expressed as a harmonic function which depends on a small detuning parameter Δ, so that the loading frequency is centered around the dimensionless circular frequency of the tether $\bar{\omega}$, i.e.:
$$\bar{F}_T(\tau) = 0 \qquad \bar{F}(\tau) = \bar{\tilde{f}}\, \sin[\bar{\omega}\,(1+\Delta)\,\tau] \tag{55}$$
In this case, the system of equations is formally decoupled, and the problem results in zero response of the tunnel, while the second row of the system is the fixed-supports forced equation of motion of the tether. This loading case will be treated in Section 5.2.3. It is also worth noticing that, differently from LC1 and LC2, this loading condition implicitly models the direct force acting on the tethers. Therefore, it inherently sees the geometrical and mechanical properties of the tether involved in the definition of the non-dimensional force amplitude $\bar{\tilde{f}}$, as expressed by Eq. (34).

Moreover, LC1 and LC2 are intended to represent a more realistic narrow-band stochastic support excitation of the tether, arising from the inertia-dominated hydrodynamic regime of the tube and its quasi-static response (see Section 1). Consequently, the PSD of the tether support motion inherits the same frequency content as the original wave load PSD, which makes the harmonic load simplification physically reasonable (see Fig. 2).

By contrast, under more realistic conditions where a nonlinear drag contribution is included in the tether forcing (LC3), an additional broadband excitation is generated. The influence of such broadband background fluctuations on nonlinear cable dynamics has been shown to significantly affect resonance, modal energy exchange, and intermittency phenomena [70]. In the present work, however, LC3 is restricted to the deterministic response associated with the dominant harmonic component of the narrow-band excitation, and this background contribution is intentionally neglected to enable the derivation of a closed-form solution.

5. Solution of the equations of motion

5.1. Ordering of the variables

This section deals with the solution of the Eq. (49) by means of the Multiple Time Scales (MTS) perturbation method. For the sake of readability, from now on, the bar symbol on the non-dimensional quantities will be removed.

Furthermore, for the sake of brevity, only the solution of the vertical motion of the SFT will be presented, and the subscript v will be omitted as well. However, it is important to notice that the solutions of systems (49) and (51) are practically the same, as the form of the equations remains unchanged. The only difference which is found for the case of the out-of plane motion is related to the transient response of the two tethers, which differ due to the activation of geometrical nonlinearities, while their steady-state response are formally identical and match the solution found for the in-plane motion.

From now on, the value of the natural circular frequency of the tube (i.e., ω_T) is selected to be representative of one of the global low-order modes of the SFT.

Moreover, the SFT global response to hydrodynamic loading being quasi-static (see Section 1), the following statement about the modal properties of the two substructures can be formally introduced:
$$\omega_T = \frac{\omega\, k}{\sqrt{\epsilon}} \tag{56}$$
ϵ being a small non-dimensional ordering variable and k a real number. Eq. (56) amounts to say that the ratio of the natural circular frequency of the tube (ω_T) and the natural circular frequency of the tether (ω) is a large number. Let us now introduce the following compact variables, for the sake of simplicity:
$$\eta^* = 2(\eta-\mu)\sin\theta \quad \alpha^* = \alpha\sin\theta \quad \zeta^* = \zeta\cos\theta \tag{57}$$
$$\beta^* = 3\beta \quad \tilde{\beta}^* = 3\tilde{\beta}\sin\theta \tag{58}$$
Suitable ordering of the variables reads:
$$\xi^s = \epsilon\,\hat{\xi}^s \qquad \xi_T = \epsilon\hat{\xi}_T \qquad \xi^{eq} = \epsilon\,\hat{\xi}^{eq} \implies K_{\mathrm{d}} = \epsilon\,\hat{K}_d \tag{59}$$
$$\beta^* = \epsilon\,\hat{\beta}^* \qquad \tilde{\beta}^* = \epsilon\,\hat{\tilde{\beta}}^* \qquad \nu = \epsilon\,\hat{\nu} \tag{60}$$
$$\tilde{f} = \epsilon\,\hat{\tilde{f}} \qquad c_0 = \epsilon\,\hat{c}_0 \qquad \Delta = \epsilon\,\delta \tag{61}$$
where $\delta, f, \eta^*, \alpha^*, \zeta^*$ and all the other variables with a hat are of $\mathcal{O}(1)$. Eqs. (59)–(61) formally state that damping coefficients (both structural and drag-induced), geometrical nonlinearities coefficients, external forcing on the tether, detuning coefficient (Δ) and the static stiffness coupling term c_0 are small numbers. This evidence was provided by preliminary numerical inspection of all the coefficients involved in the coupled system of equations.

5.2. Multiple timescales perturbation solution

After a proper scaling of the equations is introduced, the multiple time scales perturbation method can be applied. Let us seek for a solution expressed by the following regular ansatz (see, e.g. [71,72]):

$$w_T = w_{T,0} + \epsilon w_{T,1} + \epsilon^2 w_{T,2} + \mathcal{O}(\epsilon^3) \tag{62}$$

$$z = z_0 + \epsilon z_1 + \epsilon^2 z_2 + \mathcal{O}(\epsilon^3) \tag{63}$$

and introduce three different time scales:

$$T_0 = \tau, \qquad T_1 = \epsilon\,\tau, \qquad T_2 = \epsilon^2\,\tau \tag{64}$$

where T_0 is the so-called fast time scale, T_1 is the slow time scale, while T_2 is the “super”- slow time scale, so that: $z(\tau) = z(T_0, T_1, T_2)$ and $w_T(\tau) = w_T(T_0, T_1, T_2)$ [71,72].

It is worth noting that, the super-slow time scale T_2 is in principle needed when dealing with Mathieu-like terms, inducing parametric excitation.

5.2.1. Loading condition 1 (LC1)

The Loading Condition 1 (LC1) deals with an hydrodynamic force acting on the tunnel, which is Quasi-Simple-Resonant with the tether (see Section 4.5). Substitution of Eqs. (56)–(61) into Eq. (49) and multiplication of the first row by ϵ leads to the following system of equations:

$$\begin{cases} \epsilon\,\ddot{w}_T + 2\epsilon\sqrt{\epsilon}\,\xi_T\omega k\,\dot{w}_T + \omega^2 k^2 w_T - \epsilon\,\hat{c}_0 w_T - \epsilon\,\hat{f}\,\sin[\omega(1+\epsilon\delta)\tau] = 0 \\ \ddot{z} + 2\epsilon\,(\hat{\xi}^s + \hat{\xi}^{eq})\,\omega\dot{z} + \omega^2 z + \epsilon\,\hat{v}z^3 + \epsilon\,\hat{\beta}^* z^2 + \epsilon\,\hat{\hat{\beta}}^*\,z^2 w_T - \eta^*\,w_T z + (\alpha^* + \zeta^*)\,\ddot{w}_T = 0 \end{cases} \tag{65}$$

Substitution of Eqs. (62) and (63) into Eq. (65) leads to the full system of equations in the three time scales (which is not reported here, for the sake of conciseness). The system of Eq. (65) can be solved in a cascade manner, the response of the tunnel being quasi-static (i.e. one-way dynamic coupling between the tube and the mooring system). The solution of the first row of the system reads:

$$w_{T,0} = 0 \tag{66}$$

$$w_{T,1} = \frac{f}{k^2\omega^2}\sin\left(\omega T_0 + \delta\omega T_1\right) \tag{67}$$

$$w_{T,2} = \frac{f}{k^4\omega^2}\left(1 + \frac{\hat{c}_0}{\omega^2}\right)\sin\left(\omega T_0 + \delta\omega T_1\right) \tag{68}$$

Computing partial derivatives of the previous expressions and substituting in the second row of the system, leads to the sole perturbation equation of motion of the tether in the three time scales.The leading order problem reads:

$$\frac{\partial^2 z_0}{\partial T_0^2} + \omega^2\,z_0 = 0 \tag{69}$$

whose harmonic solution is:

$$z_0 = A(T_1, T_2)\exp(i\omega T_0) + \bar{A}(T_1, T_2)\exp(-i\omega T_0) \tag{70}$$

where $A(T_1, T_2)$ is the function controlling the slowly-varying amplitude of the motion, i is the imaginary unit and the bar symbol here denotes the complex conjugate operator. After direct substitution of Eqs. (66)–(68), and (70) into the second row of Eq. (49), the first order perturbation equation is found to be:

$$\begin{aligned} \frac{\partial^2 z_1}{\partial T_0^2} + \omega^2\,z_1 = {} & \frac{i\alpha^* f e^{-i\delta\omega T_1 - i\omega T_0}}{2k^2} - \frac{i\alpha^* f e^{i\delta\omega T_1 + i\omega T_0}}{2k^2} - \hat{\beta}^* e^{2i\omega T_0} A^2 + \frac{i f \zeta^* e^{-i\delta\omega T_1 - i\omega T_0}}{2k^2} + \\ & \frac{i f \zeta^* e^{i\delta\omega T_1 + i\omega T_0}}{2k^2} + \frac{i f \eta^* A e^{-i\delta\omega T_1}}{2k^2\omega^2} - \frac{i f \eta^* A e^{i\delta\omega T_1 + 2i\omega T_0}}{2k^2\omega^2} - \hat{v} e^{3i\omega T_0} A^3 + \\ & - 2i\,(\hat{\xi}^s + \hat{\xi}^{eq})\,\omega^2 e^{i\omega T_0} A - 2\hat{\beta}^* A\bar{A} - \frac{i f \eta^* e^{i\delta\omega T_1}\bar{A}}{2k^2\omega^2} + \frac{i f \eta^* e^{-i\delta\omega T_1 - 2i\omega T_0}\bar{A}}{2k^2\omega^2} + \\ & - 3\hat{v} e^{i\omega T_0} A^2\bar{A} + 2i\,(\hat{\xi}^s + \hat{\xi}^{eq})\,\omega^2 e^{-i\omega T_0}\bar{A} - \hat{\beta}^* e^{-2i\omega T_0}\bar{A}^2 - 3\hat{v} e^{-i\omega T_0} A\bar{A}^2 + \\ & - \hat{v} e^{-3i\omega T_0}\bar{A}^3 + 2i\omega e^{-i\omega T_0}\frac{\partial\bar{A}}{\partial T_1} - 2i\omega e^{i\omega T_0}\frac{\partial A}{\partial T_1} \end{aligned} \tag{71}$$

Let us now express the function $A(T_1, T_2)$ as a complex number in its exponential form:

$$A(T_1, T_2) = \frac{1}{2} a(T_1, T_2)\exp\left[i\theta(T_1, T_2)\right] \tag{72}$$

$$\bar{A}(T_1, T_2) = \frac{1}{2} a(T_1, T_2)\exp\left[-i\theta(T_1, T_2)\right] \tag{73}$$

with $a(T_1, T_2)$ and $\theta(T_1, T_2)$ real-valued non-dimensional amplitude and phase, respectively, depending on the slow time scales. Identifying secular terms in Eq. (71), and setting them to zero leads to the following equation (i.e. secularity condition):

$$-\frac{i\alpha^* f e^{i\delta\omega T_1}}{2k^2} - \frac{i f \zeta^* e^{i\delta\omega T_1}}{2k^2} - i\,(\hat{\xi}^s + \hat{\xi}^{eq})\,\omega^2 e^{i\theta} a - \frac{3}{8}\hat{\nu} e^{i\theta} a^3 + \omega e^{i\theta}\frac{\partial\theta}{\partial T_1} a - i\omega e^{i\theta}\frac{\partial a}{\partial T_1} = 0 \tag{74}$$

It is now necessary to separate real and imaginary parts of the previous equation, as well as passing to the usual trigonometric form of complex numbers. After suitable manipulations of the quantities, the following Amplitude Modulation Equations (AMEs) are obtained:

$$f\left(\alpha^* + \zeta^*\right)\cos\left[\delta\omega T_1 - \theta\right] + 2k^2\omega\left((\hat{\xi}^s + \hat{\xi}^{eq})\,\omega a + \frac{\partial a}{\partial T_1}\right) = 0 \tag{75}$$

$$3k^2\hat{\nu}a^3 = 4f\left(\alpha^* + \zeta^*\right)\sin\left[\delta\omega T_1 - \theta\right] + 8k^2\omega\frac{\partial\theta}{\partial T_1} a \tag{76}$$

At this stage, it is convenient to write the autonomous version of the dynamical system expressed by Eqs. (75) and (76). This can be easily done by means of the following change of variable, which has the physical interpretation of the phase of the autonomous system:

$$\gamma(T_1, T_2) = \delta\,\omega T_1 - \theta(T_1, T_2) \tag{77}$$

By numerical integration of the AMEs it is possible to check that both the amplitude and the phase reach a steady state over the slow time scales (i.e. a constant value over (T_1, T_2) after the transient response).

Dropping the term involving the derivative of both the amplitude and the new phase variable with respect to the slow time scale, the AMEs read:

$$f\left(\alpha^* + \zeta^*\right)\cos\gamma = -2k^2\omega^2\,(\hat{\xi}^s + \hat{\xi}^{eq})\,a \tag{78}$$

$$f\left(\alpha^* + \zeta^*\right)\sin\gamma = \frac{3}{4}k^2\hat{\nu}a^3 - 2k^2\omega^2\delta a \tag{79}$$

At this stage, by expressing the equivalent damping coefficient according to Eqs. (C.23)–(C.24), the AMEs become:

$$f\left(\alpha^* + \zeta^*\right)\cos\gamma + 2k^2\omega^2\left(\hat{\xi}^s a + \hat{K}_{\mathrm{d}} a^2\right) = 0 \tag{80}$$

$$f\left(\alpha^* + \zeta^*\right)\sin\gamma = \frac{3}{4}k^2\hat{\nu}a^3 - 2k^2\omega^2\delta a \tag{81}$$

Squaring both sides of Eqs. (80) and (81) and summing up member by member, a sixth degree algebraic equation in the steady state vibration amplitude is obtained, namely the Frequency Response Equation (FRE):

$$\frac{9\,\hat{\nu}^2}{4\,\omega^2}a^6 + \left(16\omega^2\hat{K}_{\mathrm{d}}{}^2 - 12\delta\hat{\nu}\right)a^4 + 32\omega^2\hat{\xi}^s\hat{K}_{\mathrm{d}}a^3 + 16\left(\delta^2 + \hat{\xi}^{s\,2}\right)\omega^2 a^2 - \frac{4f^2(\alpha^* + \zeta^*)^2}{k^4\omega^2} = 0 \tag{82}$$

Reabsorbing the ordering variable ϵ, the following FRE in the dimensionless parameters of the system is obtained:

$$\frac{9\,\nu^2}{4\,\omega^4}a^6 + \left(16K_d^2 - \frac{12\Delta\nu}{\omega^2}\right)a^4 + 32\xi^s K_{\mathrm{d}}a^3 + 16\left(\Delta^2 + \xi^{s2}\right)a^2 - \frac{4f^2(\alpha^* + \zeta^*)^2}{\omega_T^4} = 0 \tag{83}$$

The possible steady state vibration amplitudes of the system are then the real and positive roots of Eq. (82) or Eq. (83).

5.2.2. Loading condition 2 (LC2)

The LC2 deals with a hydrodynamic force acting on the tunnel, Quasi-Parametric-Resonant with the tether (see Section 4.5).

The very same procedure as described in the previous subsection, with reference to the LC1, is here repeated. Substitution of Eqs. (56)–(61) into Eq. (49) and multiplication of the first row by ϵ leads to the following system of equations:

$$\begin{cases} \epsilon\,\ddot{w}_T + 2\epsilon\sqrt{\epsilon}\,\xi_T\omega k\,\dot{w}_T + \omega^2 k^2 w_T - \epsilon\,\hat{c}_0 w_T - \epsilon\,\hat{f}\,\sin[\omega(2+\epsilon\delta)\tau] = 0 \\ \ddot{z} + 2\epsilon\,(\hat{\xi}^s + \hat{\xi}^{eq})\,\omega\dot{z} + \omega^2 z + \epsilon\,\hat{\nu}z^3 + \epsilon\,\hat{\beta}^* z^2 + \epsilon\,\hat{\hat{\beta}}^* z^2 w_T - \eta^*\,w_T z + (\alpha^* + \zeta^*)\,\ddot{w}_T = 0 \end{cases} \tag{84}$$

Substitution of Eqs. (62) and (63) into Eq. (84) leads to the full system of equations in the three time scales (which is not reported here, for the sake of conciseness). The system of Eq. (84) can be solved in a cascade manner, the response of the tunnel being quasi-static (i.e. one-way dynamic coupling between the tube and the mooring system). The solution of the first row of the system reads:

$$w_{T,0} = 0 \tag{85}$$

$$w_{T,1} = \frac{f}{k^2\omega^2}\sin\left(2\omega T_0 + \delta\omega T_1\right) \tag{86}$$

$$w_{T,2} = \frac{f}{k^4\omega^2}\left(4 + \frac{\hat{c}_0}{\omega^2}\right)\sin\left(2\omega T_0 + \delta\omega T_1\right) \tag{87}$$

Computing partial derivatives of the previous expression, and substituting in the second row of the system, leads to the sole perturbation equation of motion of the tether in the three time scales. The leading order problem is again expressed by Eq. (69), while its solutions are given by Eq. (70). After direct substitution of Eqs. (66)–(68), and (70), the first order perturbation equation is found to be:

$$\begin{aligned}\frac{\partial^2 z_1}{\partial T_0^2}+\omega^2 z_1 =&\frac{2i\alpha^* f e^{-i\delta\omega T_1-2i\omega T_0}}{k^2}-\frac{2i\alpha^* f e^{i\delta\omega T_1+2i\omega T_0}}{k^2}-\hat{\beta}^* e^{2i\omega T_0}A^2+\frac{2if\zeta^* e^{-i\delta\omega T_1-2i\omega T_0}}{k^2}+\\&-\frac{2if\zeta^* e^{i\delta\omega T_1+2i\omega T_0}}{k^2}+\frac{if\eta^* A e^{-i\delta\omega T_1-i\omega T_0}}{2k^2\omega^2}-\frac{if\eta^* A e^{i\delta\omega T_1+3i\omega T_0}}{2k^2\omega^2}-\hat{\nu}e^{3i\omega T_0}A^3+\\&-2i(\hat{\xi}^s+\hat{\xi}^{eq})\omega^2 e^{i\omega T_0}A-2\hat{\beta}^* A\bar{A}+\frac{if\eta^* e^{-i\delta\omega T_1-3i\omega T_0}\bar{A}}{2k^2\omega^2}-\frac{if\eta^* e^{i\delta\omega T_1+i\omega T_0}\bar{A}}{2k^2\omega^2}+\\&-3\hat{\nu}e^{i\omega T_0}A^2\bar{A}+2i(\hat{\xi}^s+\hat{\xi}^{eq})\omega^2 e^{-i\omega T_0}\bar{A}-\hat{\beta}^* e^{-2i\omega T_0}\bar{A}^2-\hat{\nu}\left(-e^{-3i\omega T_0}\right)\bar{A}^3+\\&+3\hat{\nu}e^{-i\omega T_0}A\bar{A}^2+2i\omega e^{-i\omega T_0}\frac{\partial\bar{A}}{\partial T_1}-2i\omega e^{i\omega T_0}\frac{\partial A}{\partial T_1}\end{aligned} \tag{88}$$

By expressing the function $A(T_1,T_2)$ as a complex number in its exponential form, according to Eqs. (72) and (73), one can identify secular terms, and the following secularity condition is retrieved:

$$-\frac{if\eta^*\rho e^{i\delta\omega T_1-i\theta}}{2k^2\omega^2}-i(\hat{\xi}^s+\hat{\xi}^{eq})\omega^2 e^{i\theta}a+\omega e^{i\theta}\frac{\partial\theta}{\partial T_1}a+\frac{3}{8}\hat{\nu}e^{i\theta}a^3-i\omega e^{i\theta}\frac{\partial a}{\partial T_1}=0 \tag{89}$$

By observing the form of Eq. (89), it can be argued that the response of the tether at $\mathcal{O}(\epsilon)$ is the same as that of a Mathieu-Duffing oscillator, since both the parametric excitation term and the cubic geometrical nonlinearities are present in the equation. Non trivial solutions of the Mathieu-Duffing equation and their stability have been recently studied in [73,74]. However, two fundamental peculiarities of the problem under investigation should be highlighted: (1) the coefficient of the parametric excitation term (i.e. η^*) is of $\mathcal{O}(1)$, while being of $\mathcal{O}(\epsilon)$ in standard forms of the equation and in any solution procedure present in the literature, to the best of the authors' knowledge; (2) the parametric excitation term includes both the coupling with the tunnel (i.e. its vertical degree of freedom), which acts as an input for the tether, and the structural response of the tether itself, in a multiplicative way, which highlights the fact that the time-varying stiffness of the tether is provided by the coupling with the tube.

Separating real and imaginary parts of the previous equation, as well as passing to the usual trigonometric form of complex numbers, leads to the following Amplitude Modulation Equations (AMEs):

$$f\eta^*\cos\left[\delta\omega T_1-2\theta\right]a+4k^2\omega^3\left((\hat{\xi}^s+\hat{\xi}^{eq})\,\omega a+\frac{\partial a}{\partial T_1}\right)=0 \tag{90}$$

$$3k^2\omega^2\hat{\nu}a^3=2f\eta^*\sin\left[\delta\omega T_1-2\theta\right]a+8k^2\omega^3\frac{\partial\theta}{\partial T_1}a \tag{91}$$

At this stage, it is convenient to write the autonomous version of the dynamical system expressed by Eqs. (75) and (76). This can be easily done by means of the following change of variable, which has the physical interpretation of the phase of the autonomous system:

$$\gamma(T_1,T_2)=\delta\,\omega T_1-2\theta(T_1,T_2) \tag{92}$$

By numerical integration of the AMEs it is possible to check that both the amplitude and the phase reach a steady state over the slow time scales (i.e. a constant value over (T_1,T_2) after the transient response).

Dropping the term involving the derivative of both the amplitude and the new phase variable with respect to the slow time scales, the AMEs read:

$$f\eta^*\cos\gamma=-4k^2\omega^4(\hat{\xi}^s+\hat{\xi}^{eq}) \tag{93}$$

$$f\eta^*\sin\gamma=\frac{3}{2}k^2\omega^2\hat{\nu}a^2-2k^2\omega^4\delta \tag{94}$$

By expressing the equivalent damping coefficient according to Eqs. (C.23)–(C.24), the AMEs become:

$$f\eta^*\cos\gamma+4k^2\omega^4\left(\hat{\xi}^s+\hat{K}_{\mathrm{d}}a\right)=0 \tag{95}$$

$$f\eta^*\sin\gamma=\frac{3}{2}k^2\omega^2\hat{\nu}a^2-2k^2\omega^4\delta \tag{96}$$

Squaring both sides of Eqs. (95) and (96) and summing up member by member, a fourth degree algebraic equation in the steady state vibration amplitude is obtained, namely the Frequency Response Equation (FRE):

$$\frac{9\hat{\nu}^2}{4\omega^2}a^4+\left(16\omega^2\hat{K}_{\mathrm{d}}{}^2-6\delta\hat{\nu}\right)a^2+32\omega^2\hat{\xi}^s\hat{K}_{\mathrm{d}}a+\left(4\delta^2+16\hat{\xi}^{s2}\right)\omega^2-\frac{f^2\eta^{*2}}{k^4\omega^6}=0 \tag{97}$$

Reabsorbing the ordering variable ϵ, the following FRE in the dimensionless parameters of the system is obtained:

$$\frac{9\nu^2}{4\omega^4}a^4+\left(16K_d^2-6\frac{\Delta\nu}{\omega^2}\right)a^2+32\xi^s K_{\mathrm{d}}a+\left(4\Delta^2+16\xi^{s2}\right)-\frac{f^2\eta^{*2}}{\omega_T^4\omega^4}=0 \tag{98}$$

The dimensionless steady state vibration amplitude a of the system is then obtained as the real and positive root of Eq. (97) or Eq. (98).

On this respect, it can be formally shown that the effect of the additional drag-induced damping closes the solution branch, i.e. results in a limited amplitude of vibration, instead of two open branches (i.e. stable and unstable) as it will happen if the tether was dry, such as stay cables in wind engineering applications (see Fig. 6).

This evidence has already been reported in the pioneering work of [75], by considering the structure modeled as a string, and, more recently, in [76–78], where the case of offshore vertical risers has been considered.

Indeed, with reference to the present work, it is noted that the structure of the FRE (i.e., Eq. (97)) markedly changes compared to the case of dry tether. For the latter case, by neglecting the nonlinear feedback term in the hydrodynamic force (i.e. setting $\hat{K}_\mathrm{d} = 0$), the following FRE is readily obtained:

$$\frac{9\hat{v}^2}{4\omega^2}a^4 - 6\delta\hat{v}a^2 + \left(4\delta^2 + 16\hat{\xi}^{s\,2}\right)\omega^2 - \frac{f^2\eta^{*2}}{k^4\omega^6} = 0 \tag{99}$$

Real positive roots of Eqs. (97) and (99) are plotted in Fig. 6 with reference to the same set of parameters.

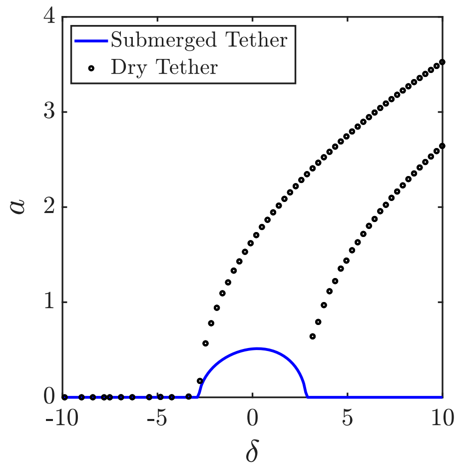

Fig. 6. Comparison of the real positive roots of Eqs. (97) (i.e., submerged tether) and (99) (i.e., dry tether) obtained for the following parameters: $\hat{v} = 1.3755$, $f = 1.4477$, $k = 0.9225$, $\omega = 1.0073$, $\eta^* = 3.4496$, $\hat{\xi} = 0.1$, $\hat{K}_d = 5.1507$ and $\epsilon = 0.01$.

It is also worth noticing that the real behavior of the solution branch obtained accounting for the amplitude-dependent damping, cannot be simply reproduced by increasing the structural damping of the system in Eq. (99). Indeed, this is a peculiar feature of submerged tethers and can only be captured with a proper modeling of the physical phenomenon itself, as it has been done in this work (see Section 3.5).

5.2.3. Loading condition 3 (LC3)

The LC3 deals with an hydrodynamic force acting on the tether, Quasi-Resonant with the tether itself (see Section 4.5). It is here recalled that, in this case, the system of Eqs. (49) is formally decoupled. The first row of the system (see Eq. (49)) admits the trivial solution only, i.e., $w_{T,0} = w_{T,1} = w_{T,2} = 0 \;\; \forall\, T_0, T_1, T_2$, while the second row of the system (see again Eq. (49)) is the fixed-support forced equation of motion of the tether. For this reason, the coupling being formally absent, the Mathieu-like term disappears from the second equation, leading to a more general Duffing oscillator, including quadratic geometrical nonlinearities:

$$\ddot{z}(\tau) + 2\epsilon\hat{\xi}\omega\dot{z}(\tau) + \omega^2 z(\tau) + \epsilon\hat{\beta}^* z^2(\tau) + \epsilon\hat{v}z^3(\tau) - \epsilon\hat{\hat{f}}\sin[\omega(1+\epsilon\delta)\tau] = 0 \tag{100}$$

Differently from LC1 and LC2 (see Sections 5.2.1 and 5.2.2), in this case it is required that the non-dimensional loading term $\tilde{f}$ is of $\mathcal{O}(\epsilon)$ (i.e. $\tilde{f} = \epsilon\hat{\hat{f}}$, see Eq. (61)). This is necessary to obtain a leading order solution which is of $\mathcal{O}(1)$.

Introduction of the three time scales and differentiation rules allow to determine the leading order problem, which is again Eq. (69), whose harmonic solution is given by Eq. (70). Substitution of Eq. (70) into the original expression allows to obtain the first order perturbation equation, which, in turn leads to the following secularity condition:

$$-\frac{1}{2}i\hat{\hat{f}}e^{i\omega\delta T_1} - i\left(\hat{\xi}^s + \hat{\xi}^{eq}\right)\omega^2 e^{i\theta}a - \frac{3}{8}\hat{v}e^{i\theta}a^3 + \omega e^{i\theta}\frac{\partial\theta}{\partial T_1}a - i\omega e^{i\theta}\frac{\partial a}{\partial T_1} = 0 \tag{101}$$

By retracing the very same passages already shown in Section 4.5, the following Amplitude Modulation Equations (AMEs) are straightforwardly derived:

$$\hat{\hat{f}}\cos\gamma + 2\omega^2\left[\hat{\xi}^s a + \hat{K}_\mathrm{d}a^2\right] = 0 \tag{102}$$

$$\hat{\hat{f}}\sin\gamma + 2\delta\omega^2 a = \frac{3}{4}\hat{v}a^3 \tag{103}$$

Squaring both sides of Eqs. (102) and (103) and summing up member by member, a sixth degree algebraic equation in the steady state vibration amplitude is obtained, namely the Frequency Response Equation (FRE):

$$\frac{9\,\hat{\nu}^2}{4\,\omega^2}\,a^6 + \left(16\omega^2 \hat{K}_{\mathrm{d}}^{\,2} - 12\delta\hat{\nu}\right)a^4 + 32\omega^2\hat{\xi}^s\hat{K}_{\mathrm{d}}a^3 + 16\left(\delta^2 + \hat{\xi}^{s\,2}\right)\omega^2 a^2 - \frac{4\hat{\tilde{f}}^2}{\omega^2} = 0 \tag{104}$$

Eq. (104) has the same structure as Eq. (82). Indeed, they both stem from a Duffing-type oscillator which is excited close to its natural frequency. However, a substantial difference between the two is that Eq. (82) incorporates the effect of the coupling with the tunnel, through the coefficients governing the inertial support motion (i.e. α^* and ζ^*) and the frequency ratio k. On the contrary, Eq. (104) is essentially describing the forced response of the tether with fixed supports, totally decoupled from the tunnel.

Reabsorbing the ordering variable ϵ, the following FRE in the dimensionless parameters of the system is obtained:

$$\frac{9\,\nu^2}{4\,\omega^4}\,a^6 + \left(16K_d^2 - 12\frac{\Delta\nu}{\omega^2}\right)a^4 + 32\xi^s K_{\mathrm{d}}a^3 + 16\left(\Delta^2 + \xi^{s2}\right)a^2 - \frac{4\tilde{f}^2}{\omega^4} = 0 \tag{105}$$

The possible steady state vibration amplitude are the real and positive roots of Eq. (104) or Eq. (105).

6. Application example

Let us consider a steel hollow-core circular cross-section tether having external diameter $D_o = 1.950$ m, profile thickness $t_o = 0.065$ m and chord length $L_0 = 403.05$ m. The material properties are set to: $E = 210$ GPa, $f_y = 450$ MPa, $\rho_s = 7850$ kg/m^3 and $\rho_w = 1000$ kg/m^3. This result in a cross-section area $A_0 = 0.3849$ m^2, virtual mass per unit of length $\gamma_v = 6005$ kg/m and buoyancy ratio br $= 0.987$. The tunnel natural circular frequency is set to $\omega_T = 3.889$ rad/s, and it is representative of one of the 5 closely spaced global vibration modes of the SFT proposed for the Messina Strait crossing, in Italy, described in [1]. The structural damping coefficient of the tunnel and of tethers are respectively set to $\xi_T = 0.05$ and $\xi^s = 0.001$. Additionally, the characteristic quantities associated with a dimensionless tether pretension value of $\eta_0 = 10\%$ are $L_c = 0.44$ m and $\omega_c = 0.4185$ rad/s, while those associated with $\eta_0 = 20\%$ are $L_c = 0.22$ m and $\omega_c = 0.592$ rad/s.

6.1. Numerical validation

In this section, a numerical validation of the different perturbation solutions is presented.

Numerical simulations are performed in the time domain, by solving system of Eq. (49) under the three loading conditions (see Section 4.5) and for different values of the mistuning coefficient. A fifth-order Runge-Kutta implicit algorithm with adaptive time steeping (*ode45* in Matlab environment) is adopted. A time duration of 5000 s is selected for each time domain analysis, which is sufficiently long to reach steady-state conditions for the prescribed value of damping. The value of the steady-state vibration amplitude is then stored and plotted as a function of the detuning parameter of the load.

Figs. 7–9 show the comparison of the numerical results with the perturbation solutions, for LC1, LC2 and LC3, respectively. Excellent agreement is found within the range of validity of the adopted hypotheses (see Eqs. (59)–(61)).

Conversely, the accuracy of the perturbation solution is observed to deteriorate slightly as the tether pretension decreases (i.e. for $\eta_0 < 10\%$) and as the detuning parameter increases (i.e., for $|\delta| > 10$). The reduction in accuracy observed for LC1 is more pronounced than that for LC3, as the pretension decreases (compare Fig. 7(b) with Fig. 9(b) in the region $|\delta| > 10$).

However, it should be noted that the perturbation solution has been derived under the assumption $\delta = \mathrm{ord}(1)$; therefore values of $|\delta| > 10$ lie at the boundary of its formal range of validity.

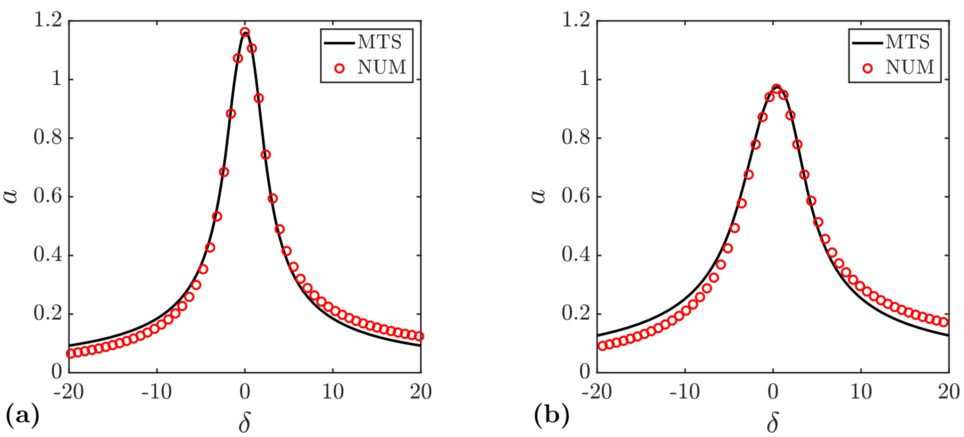

Fig. 7. Comparison of the steady state vibration amplitude obtained with the numerical solution of system (49), subject to LC1 (NUM, see Eq. (53)), and the perturbation solution (MTS, see Eq. (82)). Fixed parameters: $\theta = 135°$, $f = 1.441$, $C_D = 1.0$. Additionally $\eta_0 = 20\%$, $\lambda^2 = 0.022$, $k = 0.656$, $\omega = 1.0009$ and $K_{\mathrm{d}} = 0.0129$ for subfig. (a), while $\eta_0 = 10\%$, $\lambda^2 = 0.178$, $k = 0.923$, $\omega = 1.0073$ and $K_{\mathrm{d}} = 0.0257$ for subfig. (b).

By direct inspection of the structure of the perturbation solutions (cf. Eqs. (82) and (104)), it can be stated that this discrepancy should be solely attributed to the magnitude of the coefficients governing the inertial supports motion (i.e α^* and ζ^*) and not to those controlling the geometrical nonlinearities of the system (i.e., $\hat{\nu}$).

Moreover, the closed-form solutions are not able to capture the asymmetry in the response with respect to the sign of the detuning coefficient. This is particularly evident in Fig. 7 (for $\eta_0 = 10\%$) and can be attributed to the linearization of the drag force contribution and its consequent treatment as an equivalent damping coefficient of the system (see Section 3.5 and App. C).

Additionally, as a peculiar behavior of the LC2, it is noted that, while the perturbation solution predicts zero vibration amplitude outside the triggered region, the numerical simulations reveal that a small vibration is still observed. The latter goes to zero by further increasing the absolute value of the detuning parameter. For this reason, the loci of vibration amplitude found with the perturbation solution have been shifted upward (by $a = 0.05$) in Fig. 8, to cope with the numerical evidence, for the sake of comparison.

Overall, a very good agreement between the closed-form solution and the numerical results is found for all the considered loading cases.

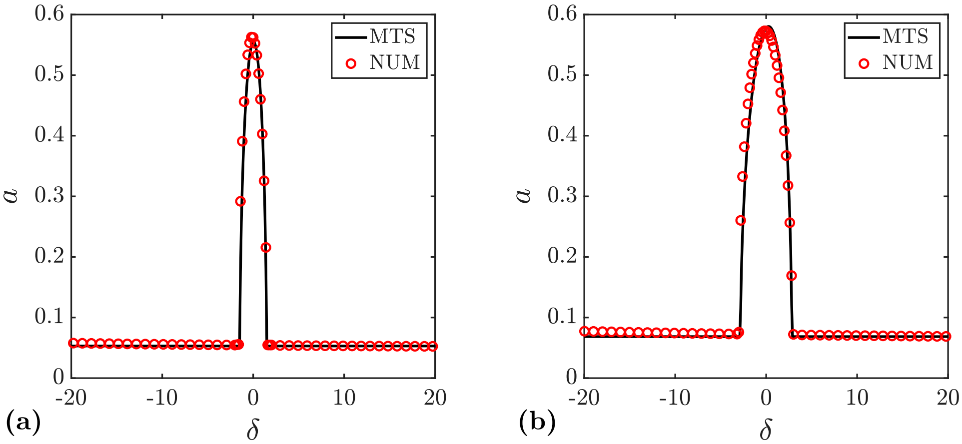

Fig. 8. Comparison of the steady state vibration amplitude obtained with the numerical solution of system (49), subject to LC2 (NUM, see Eq. (54)), and the perturbation solution (MTS, see Eq. (97)). Fixed parameters: $\theta = 135°$, $f = 1.441$, $C_D = 1.0$. Additionally $\eta_0 = 20\%$, $\lambda^2 = 0.022$, $k = 0.656$, $\omega = 1.0009$ and $K_d = 0.0129$ for subfig. (a), while $\eta_0 = 10\%$, $\lambda^2 = 0.178$, $k = 0.923$, $\omega = 1.0073$ and $K_d = 0.0257$ for subfig. (b).

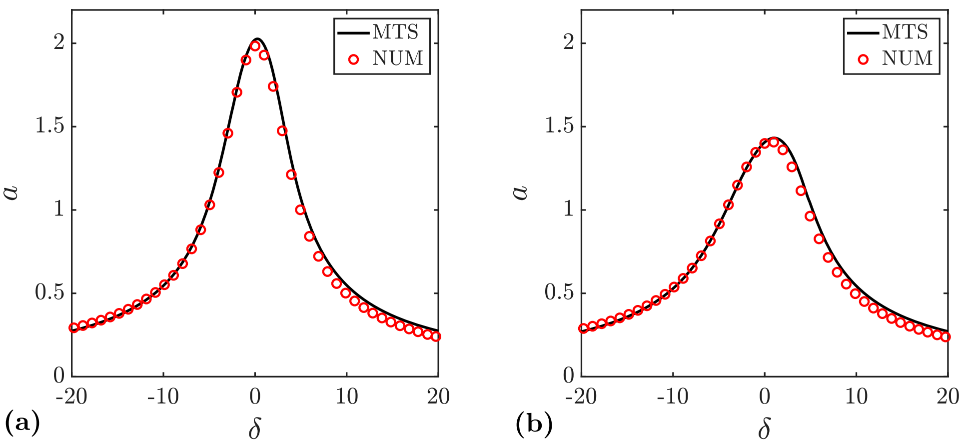

Fig. 9. Comparison of the steady state vibration amplitude obtained with the numerical solution of system (49), subject to LC3 (NUM, see Eq. (55)), and the perturbation solution (MTS, see Eq. (104)). Fixed parameters: $\theta = 135°$, $\tilde{f} = 0.107$, $C_D = 1.0$. Additionally $\eta_0 = 20\%$, $\lambda^2 = 0.022$, $k = 0.656$, $\omega = 1.0009$ and $K_d = 0.0129$ for subfig. (a), while $\eta_0 = 10\%$, $\lambda^2 = 0.178$, $k = 0.923$, $\omega = 1.0073$ and $K_d = 0.0257$ for subfig. (b).

The validation presented herein is performed against direct numerical integration of the same reduced-order equations of motion. Although this constitutes a necessary step to verify the accuracy and convergence of the asymptotic approximation, it does not represent a full validation of the underlying physical model against higher-fidelity simulations or experimental data.

6.2. Parametric analyses

In this section, the influence of the drag coefficient C_D, inclination angle θ, Irvine's parameter λ^2 and external forces f and $\tilde{f}$ on the steady-state amplitude of oscillations is investigated for the three different loading conditions (LC1,LC2 and LC3, see Section 4.5), using the different perturbation solutions developed in Section 5.2. These parameters formally represent the minimum number of dimensionless groups which permit to fully describe the dynamics of the system (see Eqs. (B.1)–(B.8) in App. B). Both the manifold of the response and its contour plot are represented in Figs. 10–21.

Figs. 10–12 depict the influence of the drag coefficient of the tether on the amplitude of vibrations. They clearly show that the dynamic response of the tether, subject to loading scenario 1 and 3 can be assimilated to that of a Duffing oscillator with hardening behavior. On the contrary, as already anticipated, loading scenario 2 delivers a Mathieu-Duffing type response, with hardening behavior as well. The drag coefficient negatively correlates with the amplitude of oscillations for LC1 and LC2. In particular, the nonlinear increase of vibration amplitude observed passing from high values to low values of C_D is faster for LC2, compared to LC1. This highlights the sensitivity of the Mathieu-Duffing equation to the damping of the system. Highest vibration amplitudes are observed for small positive values of the detuning parameter (i.e., δ around $2-3$), leading non a nonlinear and non-symmetric response. Finally, LC3 practically shows a constant vibration amplitude as a function of the drag coefficient. This is because of the linear dependence of both the external forcing and of the added-water damping upon the drag coefficient of the tether (see App. C). On the contrary, for both LC1 and LC2, the loading acting on the tunnel is assumed of inertial-type only (see Sections 2 and 4.5), leading to a nonlinear dependence of the tether vibration amplitude on the drag coefficient of the tether itself.

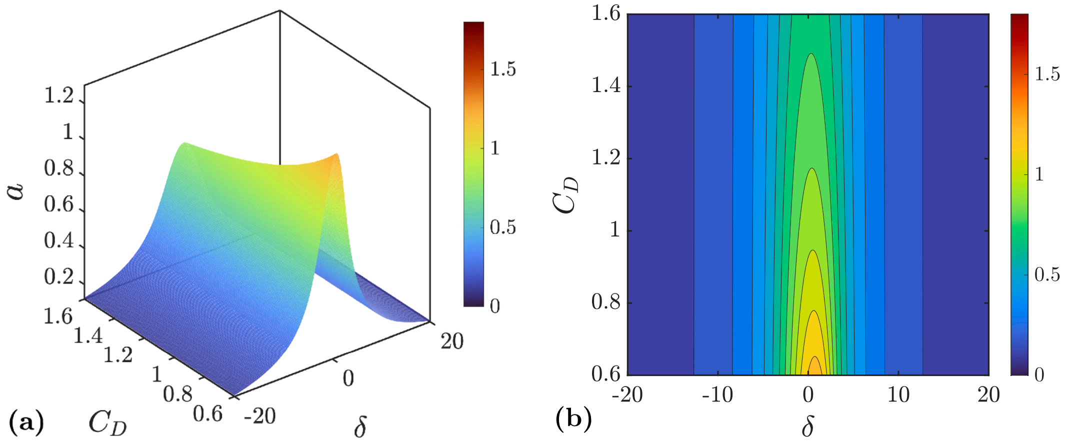

Fig. 10. Manifold (a) and contour plot (b) of the non-dimensional steady state vibration amplitudes a predicted by the perturbation solution, as a function of the detuning parameter δ and of the drag coefficient C_D, for the LC1. Fixed parameters: $\theta = 135°$, $\eta_0 = 10\%$, $\lambda^2 = 0.178$, $k = 0.923$, $f = 1.441$. The reader is referred to the online version of the manuscript for colors.

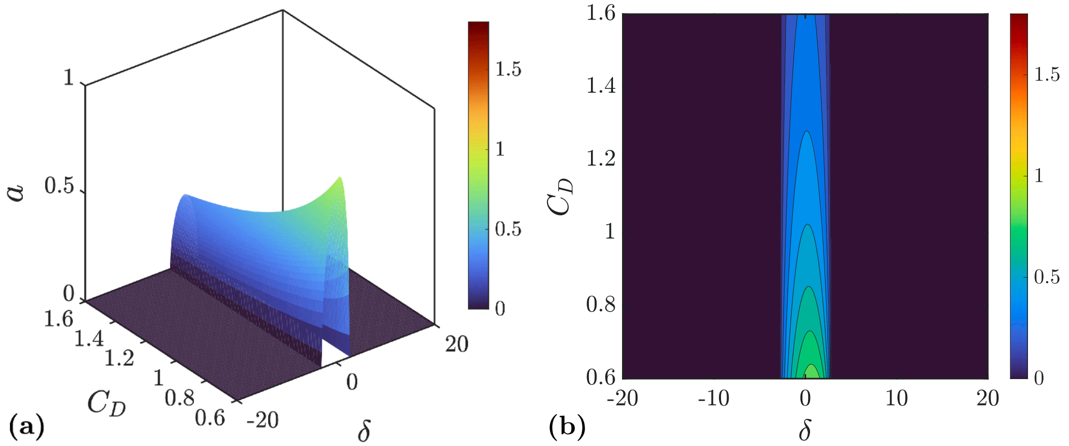

Fig. 11. Manifold (a) and contour plot (b) of the non-dimensional steady state vibration amplitudes a predicted by the perturbation solution, as a function of the detuning parameter δ and of the drag coefficient C_D, for the LC2. Fixed parameters: $\theta = 135°$, $\eta_0 = 10\%$, $\lambda^2 = 0.178$, $k = 0.923$, $f = 1.441$. The reader is referred to the online version of the manuscript for colors.

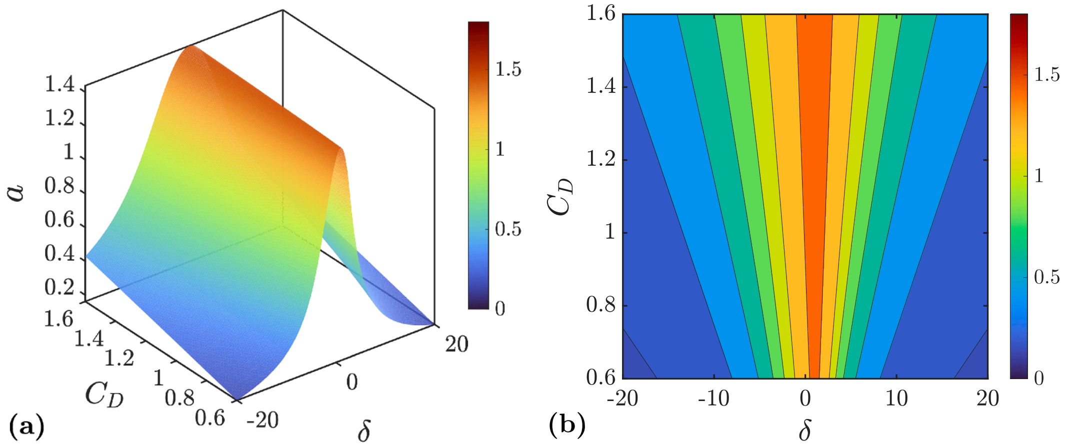

Fig. 12. Manifold (a) and contour plot (b) of the non-dimensional steady state vibration amplitudes a predicted by the perturbation solution, as a function of the detuning parameter δ and of the drag coefficient C_D, for the LC3. Fixed parameters: $\theta = 135°$, $\eta_0 = 10\%$, $\lambda^2 = 0.178$, $k = 0.923$, $b = 1.1934$. The reader is referred to the online version of the manuscript for colors.

Figs. 13–15 depict the influence of the inclination angle on the amplitude of vibrations. The maximum vibration amplitude is attained for the case of vertical tethers (i.e., $\theta = 90°$) as far as the loading condition 2 is concerned, while it is reached for values of θ around 60° and 120°, if the loading case 1 is considered. Moreover, when dealing with the direct loading acting on the tether (i.e., LC3), it is noted that the maximum vibration amplitude is obtained for a wider region of the parameter space, i.e., for value of θ in between $80° - 100°$. The provided ranges of inclination angle are referred to the region close to resonance phenomena, i.e. for δ in between $2 - 3$, which again underlines a slightly nonlinear hardening-type behavior. As far as $|\delta|$ is increased, vibration amplitudes rapidly decrease for loading cases 1 and 2, while they tend to go to zero more slowly if LC3 is concerned.

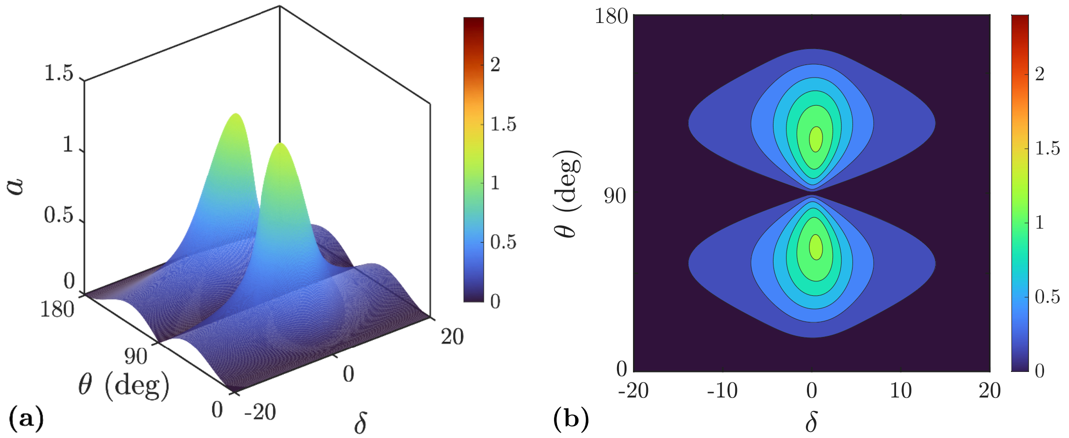

Fig. 13. Manifold (a) and contour plot (b) of the non-dimensional steady state vibration amplitudes a predicted by the perturbation solution, as a function of the detuning parameter δ and of the inclination angle θ, for the LC1. Fixed parameters: $C_D = 1$, $\eta_0 = 10\%$, $f = 1.441$. The reader is referred to the online version of the manuscript for colors.

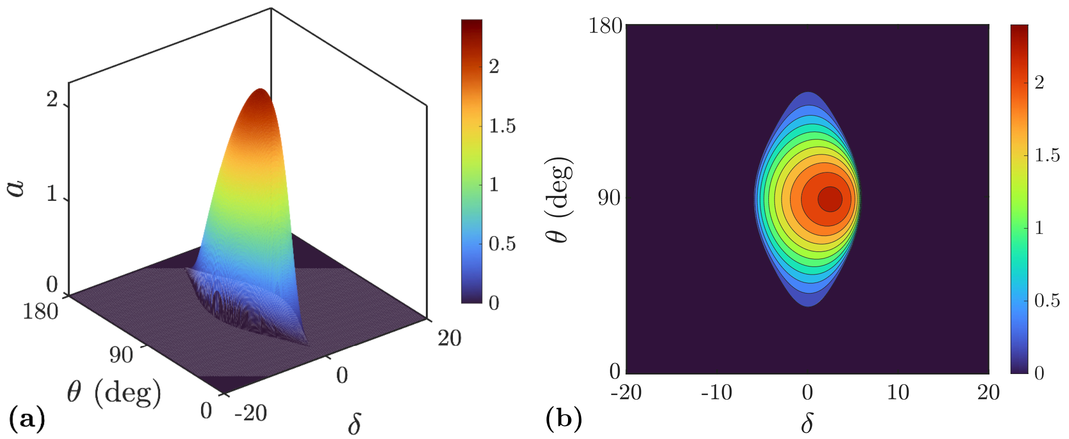

Fig. 14. Manifold (a) and contour plot (b) of the non-dimensional steady state vibration amplitudes a predicted by the perturbation solution, as a function of the detuning parameter δ and of the inclination angle θ, for the LC2. Fixed parameters: $C_D = 1$, $\eta_0 = 10\%$, $f = 1.441$. The reader is referred to the online version of the manuscript for colors.

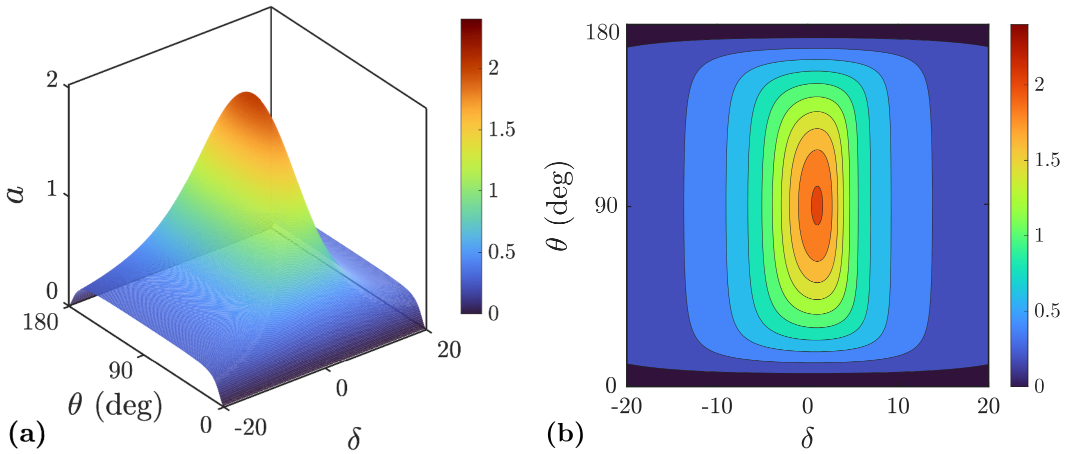

Fig. 15. Manifold (a) and contour plot (b) of the non-dimensional steady state vibration amplitudes a predicted by the perturbation solution, as a function of the detuning parameter δ and of the inclination angle θ, for the LC3. Fixed parameters: $C_D = 1$, $\eta_0 = 10\%$ and $B = 0.22$ m/s (see App. C). The reader is referred to the online version of the manuscript for colors.

Figs. 16–18 depict the influence of the Irvine's parameter λ^2 on the tether dimensionless vibration amplitude, as a function of the detuning parameter. As λ^2 increases, geometrical nonlinearities increase as well, giving rise to a severe nonlinear hardening-type response, with associated increment of the dynamic vibration amplitude, if compared to the reference case (i.e., the one associated to $\eta_0 = 10\%$ and $\lambda^2 = 0.178$). As $\lambda^2 \to 0$, the linear, perfectly-symmetric response is retrieved, and a lower vibration amplitude is encountered.

Moreover, Fig. 17 shows that for decreasing values of λ^2, the region associated to limited vibration amplitudes tend to become narrower and narrower, up to total closure as $\lambda^2 \to 0$.

Figs. 19–21 show the influence of the external force amplitude f ($\tilde{f}$) on the tether dimensionless vibration amplitude, as a function of the detuning parameter. The range of values in which f and $\tilde{f}$ are plotted, can be associated to intervals of the water particles acceleration (at the tube's centroid) and water particle normal velocity (acting at the tether's midspan) respectively equal to $\dot{u} \in [0, 0.25]$ m/s^2 and $u_\perp \in [0, 0.35]$ m/s.

It can be easily recognized that the external force amplitude has an effect similar to Irvine's parameter λ^2 on the non-dimensional vibration amplitude. As f or $\tilde{f}$ increases, an increase in the geometrical nonlinear (hardening-type) behavior is observed.

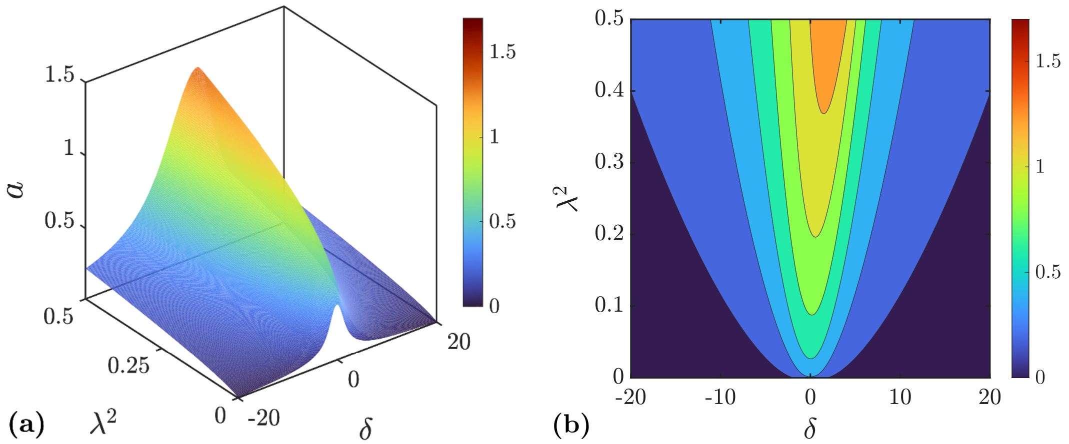

Fig. 16. Manifold (a) and contour plot (b) of the non-dimensional steady state vibration amplitudes a predicted by the perturbation solution, as a function of the detuning parameter δ and of the Irvine's parameter λ^2, for the LC1. Fixed parameters: $\theta = 135°$, $C_D = 1$ and f is associated to a water particle acceleration $\dot{u} = 0.08$ m/s^2 at the tube centroid. The characteristic length is computed for a value of $\eta_0 = 10\%$ and kept fixed for all the different analyses ($L_c = 0.44$ m). The reader is referred to the online version of the manuscript for colors.

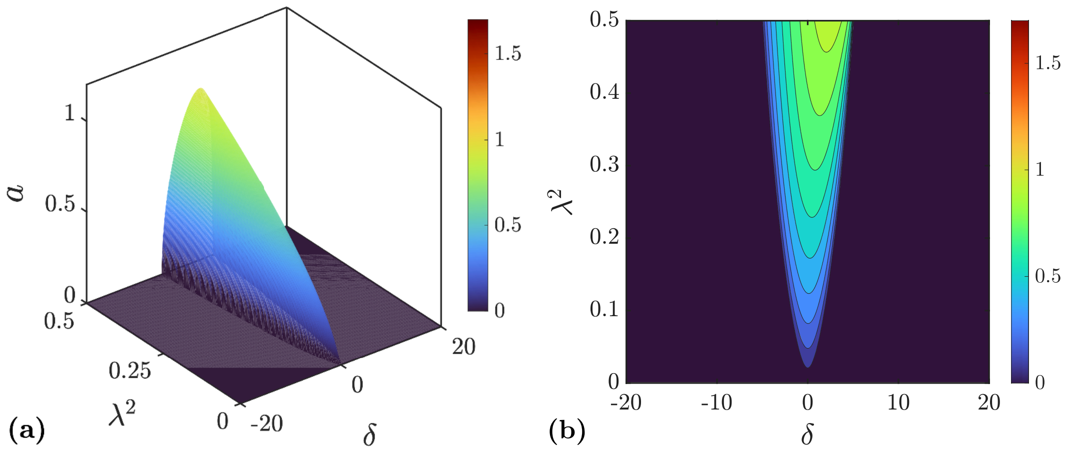

Fig. 17. Manifold (a) and contour plot (b) of the non-dimensional steady state vibration amplitudes a predicted by the perturbation solution, as a function of the detuning parameter δ and of the Irvine's parameter λ^2, for the LC2. Fixed parameters: $\theta = 135°$, $C_D = 1$ and f is associated to a water particle acceleration $\dot{u} = 0.08$ m/s^2 at the tube centroid. The characteristic length is computed for a value of $\eta_0 = 10\%$ and kept fixed for all the different analyses ($L_c = 0.44$ m). The reader is referred to the online version of the manuscript for colors.

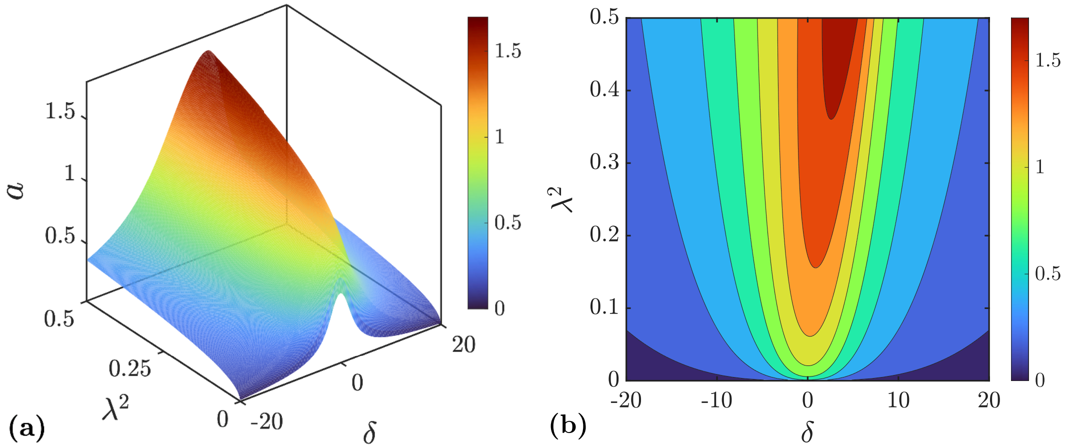

Fig. 18. Manifold (a) and contour plot (b) of the non-dimensional steady state vibration amplitudes a predicted by the perturbation solution, as a function of the detuning parameter δ and of the Irvine's parameter λ^2, for the LC3. Fixed parameters: $\theta = 135°$, $C_D = 1$ and $\tilde{f}$ is associated to a constant amplitude of water velocity $B = 0.22$ m/s (see App. C). The characteristic length is computed for a value of $\eta_0 = 10\%$ and kept fixed for all the different analyses ($L_c = 0.44$ m). The reader is referred to the online version of the manuscript for colors.

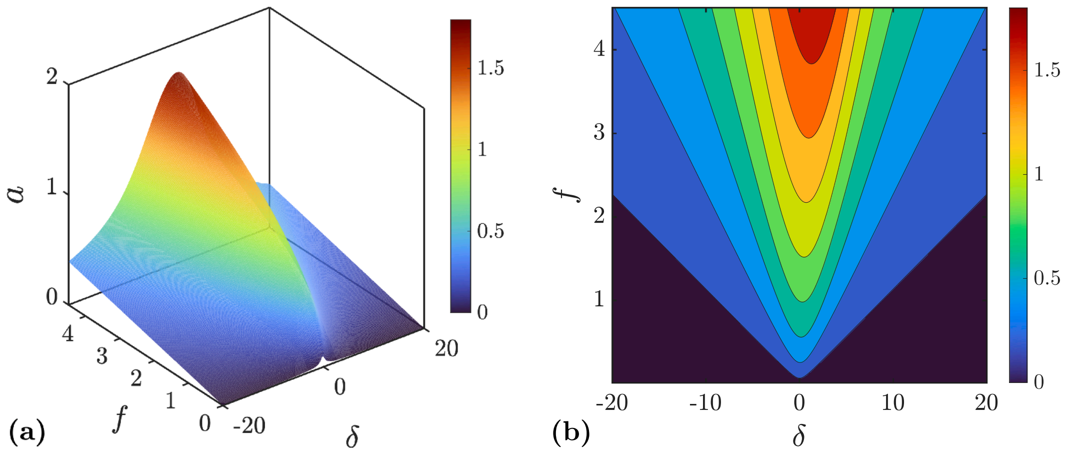

Fig. 19. Manifold (a) and contour plot (b) of the non-dimensional steady state vibration amplitudes a predicted by the perturbation solution, as a function of the detuning parameter δ and of the force amplitude f, for the LC1. Fixed parameters: $\theta = 135°$, $C_D = 1$, $k = 0.923$, $\eta_0 = 10\%$ and $\lambda^2 = 0.178$. The reader is referred to the online version of the manuscript for colors.

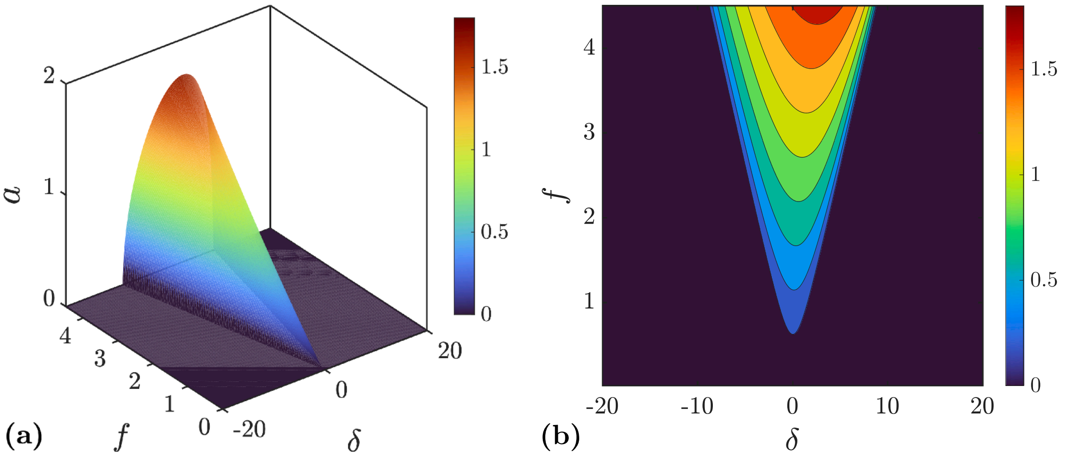

Fig. 20. Manifold (a) and contour plot (b) of the non-dimensional steady state vibration amplitudes a predicted by the perturbation solution, as a function of the detuning parameter δ and of the force amplitude f, for the LC2. Fixed parameters: $\theta = 135°$, $C_D = 1$, $k = 0.923$, $\eta_0 = 10\%$ and $\lambda^2 = 0.178$. The reader is referred to the online version of the manuscript for colors.

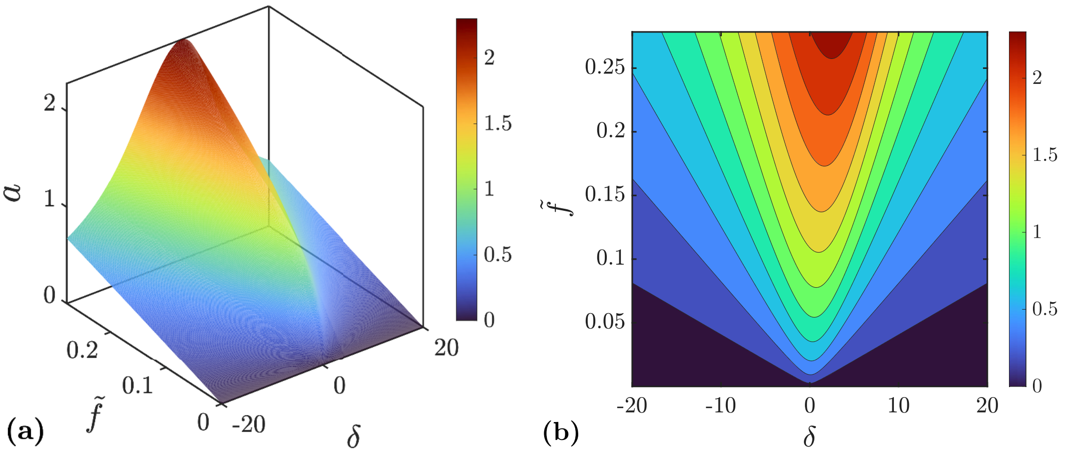

Fig. 21. Manifold (a) and contour plot (b) of the non-dimensional steady state vibration amplitudes a predicted by the perturbation solution, as a function of the detuning parameter δ and of the force amplitude $\tilde{f}$, for the LC3. Fixed parameters: $\theta = 135°$, $C_D = 1$, $k = 0.923$, $\eta_0 = 10\%$ and $\lambda^2 = 0.178$. The reader is referred to the online version of the manuscript for colors.

7. Conclusions

The dynamic response of the anchoring elements for Submerged Floating Tunnels (SFTs) subject to hydrodynamic loads has been investigated. A 2D cross-sectional model of the SFT has been developed, by describing the tube as a 2 °-of-freedom rigid body and neglecting its torsional behavior. The values of tube mass and stiffnesses have been selected to be representative of the modal quantities characterizing the cluster of low-order global modes of SFT.

The anchoring elements have been described with a reduced-order model specifically developed for inclined submerged tethers, accounting for geometrical nonlinearities and supports motion.

Inspection of the system of equations governing the coupled dynamic response of the cross-sectional model revealed the smallness of several parameters, suggesting that (1) coupling effects are one-way only (vibrations are transmitted from the tunnel to the anchoring elements and not vice versa) and that (2) heave and sway responses are almost decoupled.

These considerations justified the study of the uncoupled heave and sway equations of motion.

Three different loading conditions have been considered, suitably identified from the classification of the motion regimes of the SFT under hydrodynamic loads, including indirect loading on the tethers transmitted by the inertia force acting on the tunnel (both in quasi-simple and quasi-parametric resonance conditions with the tether) as well as direct loading on the tethers modeled as a drag-dominated hydrodynamic force.

Moreover, the expression of an equivalent viscous modal damping coefficient has been derived by linearizing the drag force acting on the anchoring elements, capturing the additional dissipative effect induced by the fluid-structure interaction.

Given the quasi-static global response of the SFT under hydrodynamic loads, closed-form analytical solutions of the tether vibration amplitude have been derived thanks to the application of the Multiple Time Scales (MTS) perturbation method, for the three different loading conditions.

After a numerical validation of the closed-form expressions was performed, extensive parametric analyses in the space of technically relevant parameters of the tethers have been carried out. Results clearly show the effect of the drag coefficient, inclination angle, Irvine's parameter and force amplitudes on the response curves.

The work allowed for a complete characterization of the dynamic response of the anchoring elements subject to hydrodynamic loading conditions considering the coupling with the tube, serving as a fundamental tool in the optimization of the mooring system's parameters for the conceptual design phase of seabed-anchored SFTs.

CRediT authorship contribution statement

Stefano Corazza: Writing – review & editing, Writing – original draft, Visualization, Validation, Software, Methodology, Investigation, Formal analysis; **Francesco Foti:** Writing – review & editing, Writing – original draft, Visualization, Supervision, Software, Methodology, Investigation, Conceptualization; **Luca Martinelli:** Writing – review & editing, Supervision, Methodology, Conceptualization; **Vincent Denoël:** Writing – review & editing, Supervision, Methodology, Formal analysis, Conceptualization.

Declaration of competing interest

The authors declare that they have no known competing financial interests or personal relationships that could have appeared to influence the work reported in this paper.

Acknowledgments

The authors would like to thank Prof. Federico Perotti from the Department of Civil and Environmental Engineering of Politecnico di Milano for the many fruitful discussions.

Data availability

Data will be made available on request.

Appendix A. Coefficients of the tether equation of motion

In this Appendix, the expressions of the coefficients appearing in Eq. (26) are reported:

$$m = \frac{\gamma_v L_0}{2} \qquad \zeta = \frac{\gamma_v L_0}{\pi} \qquad v = \frac{E A_0 \pi^4}{8 L_0^3} \tag{A.1}$$

$$\alpha = \frac{24\gamma_v w_s (1-\mathrm{br}) L_0^2 \cos\theta}{(12+\lambda^2)\pi^3 T_0 \varepsilon_0} \qquad \omega = \frac{\pi}{L_0}\sqrt{\frac{T_0}{\gamma_v} + \frac{8T_0\,\lambda^2}{\pi^4\,\gamma_v}} \tag{A.2}$$

$$\eta = \frac{3EA_0\,\pi^2}{(12+\lambda^2)L_0^2} \qquad \mu = \frac{48 w_s^2 (1-\mathrm{br})\cos^2\theta}{(12+\lambda^2)\pi^2 T_0 \varepsilon_0^2} \tag{A.3}$$

$$\beta = \frac{2\,\pi w_s (1-\mathrm{br})\cos\theta}{4L_0\varepsilon_0} \qquad \tilde{\beta} = \frac{6\pi w_s (1-\mathrm{br})\cos\theta}{(12+\lambda^2)L_0^2\varepsilon_0^2} \tag{A.4}$$

Appendix B. Non-dimensional coefficients of the tether equation of motion

In this Appendix, the expressions of the coefficients appearing in Eqs. (30) and (44) are reported. The quantities L_c and ω_c denote, respectively a characteristic length and circular frequency (see Eqs. (28) and (29)). For the meaning of all the quantities, please refer both to App. A and the body of the text.

$$\bar{\omega} = \frac{\omega}{\omega_c} = \sqrt{1 + \frac{8\lambda^2}{\pi^4}} \tag{B.1}$$

$$\bar{\zeta} = \frac{\zeta}{m} = \frac{2}{\pi} \tag{B.2}$$

$$\bar{\alpha} = \frac{\alpha}{m} = \frac{48\cos\theta}{\pi^3}\,\frac{\Gamma}{(12+\lambda^2)\,\varepsilon_0} \tag{B.3}$$

$$\bar{v} = \frac{v\,L_c^2}{\omega_c^2\,m} = \frac{\pi^2}{256\cos^2\theta}\,\lambda^2 \tag{B.4}$$

$$\bar{\eta} = \frac{\eta\,L_c}{\omega_c^2\,m} = \frac{3}{4}\,\frac{\Gamma}{(12+\lambda^2)\,\epsilon_0} \tag{B.5}$$

$$\bar{\mu} = \frac{\mu\,L_c}{\omega_c^2\,m} = \frac{12}{\pi^4}\,\lambda^2\,\frac{\Gamma}{(12+\lambda^2)\,\epsilon_0} \tag{B.6}$$

$$\bar{\beta} = \frac{\beta\,L_c}{\omega_c^2\,m} = \frac{1}{8\pi\cos\theta}\,\lambda^2 \tag{B.7}$$

$$\bar{\tilde{\beta}} = \frac{\tilde{\beta}\,L_c^2}{\omega_c^2\,m} = \frac{6}{32\pi\cos\theta}\,\lambda^2\,\frac{\Gamma}{(12+\lambda^2)\,\epsilon_0} \tag{B.8}$$

$$\bar{\omega}_{T_v} = \frac{\omega_{T_v}}{\omega_c} \qquad \bar{\omega}_{T_h} = \frac{\omega_{T_h}}{\omega_c} \tag{B.9}$$

$$\bar{F} = \frac{F}{m\,\omega_c^2\,L_c} \qquad \bar{F}_{T_v} = \frac{F_{T_v}}{m_T\,\omega_c^2\,L_c} \qquad \bar{F}_{T_h} = \frac{F_{T_h}}{m_T\,\omega_c^2\,L_c} \tag{B.10}$$

Appendix C. Linearization of the drag force

This Appendix deals with the linearization of the drag force per unit of length acting on the inclined anchoring elements. By neglecting the steady current profile and considering drag-dominated effects, Morison force per unit of length acting on the tether reads:

$$q(x,t) = C_D \rho_w \frac{D_o}{2} |u_\perp(x,t) - \dot{w}(x,t)| \left(u_\perp(x,t) - \dot{w}(x,t)\right) \tag{C.1}$$

where $u_\perp(x,t)$ is the water particle velocity normal to the tether's axis, and $\dot{w}(x,t)$ the structural velocity. In the spirit of the "Absolute Velocity Approach", the drag force caused by a wave on an oscillating cylinder can be approximated as the superposition of a force caused by a wave on a stationary cylinder (i.e., fixed) and a force exerted on an oscillating cylinder in still water (i.e., considering $u_\perp(x,t) = 0$), that is:

$$q(x,t) \simeq C_D \rho_w \frac{D_o}{2} |u_\perp(x,t)| u_\perp(x,t) - C_D \rho_w \frac{D_o}{2} |\dot{w}(x,t)| \dot{w}(x,t) \tag{C.2}$$

By recalling Eq. (21), one simply has:

$$q(x,t) \simeq C_D \rho_w \frac{D_o}{2} |u_\perp(x,t)| u_\perp(x,t) - C_D \rho_w \frac{D_o}{2} |\dot{z}(t)\psi(x)| \dot{z}(t)\psi(x) \tag{C.3}$$

$\psi(x)$ being the shape function expressed by Eq. (22). It is worth noticing that Eq. (C.3) holds only if the quasi-static velocity components of the tether are strictly zero (i.e. for Loading Condition 3 (LC3)). For what concerns Loading Conditions 1 (LC1) and 2 (LC2), a small approximation is therefore introduced, by neglecting such quasi-static velocity contributions. The total in-plane physical velocity of the tether is therefore assumed to be coincident with the its modal component.

A deterministic linearization technique is hereafter adopted to address both terms. Let us start from the direct forcing term in the fluid velocity. To this aim, let us express the normal component of the wave particle velocity as a harmonic function, resonant with the natural circular frequency of the tether:

$$u_\perp = B\sin(\omega t) \tag{C.4}$$

As a consequence, steady-state solution of the equation of motion is sought in the form:

$$z = A\cos(\omega t + \theta) \tag{C.5}$$

By adopting a non-dimensional formulation, and indicating with an dot the derivative with respect to the non-dimensional time, one has:

$$\bar{u}_\perp = \bar{b}\sin(\bar{\omega}\tau) \tag{C.6}$$

$$\bar{z} = \bar{a}\cos(\bar{\omega}\tau + \Phi) = \bar{a}\cos(\Theta) \tag{C.7}$$

$$\dot{\bar{z}} = -\bar{a}\bar{\omega}\sin(\bar{\omega}\tau + \Phi) = -\bar{a}\bar{\omega}\sin(\Theta) \tag{C.8}$$

where $\bar{u}_\perp = u_\perp/(L_c\omega_c)$ is a non-dimensional water particle velocity, $\bar{a} = A/L_c$ and $\bar{b} = B/(L_c\omega_c)$ are the non-dimensional base values of displacement and water particle velocity, respectively, while Φ is a phase angle. The non-dimensional equation of motion of the forced fixed-supports tether reads:

$$\ddot{\bar{z}}(\tau) + 2\xi^s\bar{\omega}\dot{\bar{z}}(\tau) + \bar{\omega}^2\bar{z}(\tau) + 3\bar{\beta}\bar{z}^2(\tau) + \bar{v}\bar{z}^3(\tau) = \bar{\Upsilon}_1\,|\bar{u}_\perp(\tau)|\bar{u}_\perp(\tau) - \bar{\Upsilon}_2\,|\dot{\bar{z}}(\tau)|\dot{\bar{z}}(\tau) \tag{C.9}$$

where ξ^s is the structural modal damping coefficient, while the introduced $\bar{\Upsilon}_1$ and $\bar{\Upsilon}_2$ constants are defined as:

$$\bar{\Upsilon}_1 = \frac{1}{2}C_D\rho_w D_o\,\frac{2L_0}{\pi^2 T_0 L_c}\int_0^{L_0}\psi(x)\,L_c^2\omega_c^2\,dx = \frac{2C_D\rho_w D_o L_c}{\pi\gamma_v} \tag{C.10}$$

$$\bar{\Upsilon}_2 = \frac{1}{2}C_D\rho_w D_o\,\frac{2L_0}{\pi^2 T_0 L_c}\int_0^{L_0}\psi^3(x)\,L_c^2\omega_c^2\,dx = \frac{4C_D\rho_w D_o L_c}{3\pi\gamma_v} \tag{C.11}$$

and are straightforwardly defined recalling the expression of the dimensionless generalized component of the external force (Eq. (B.10)).

Following a classical Fourier Series representation, and keeping only the first term of the series expansion, substitution of Eq. (C.6) in Eq. (C.9) allows to express the forcing term proportional to the fluid velocity as:

$$\bar{\Upsilon}_1\bar{b}^2\,\sin(\bar{\omega}\tau)|\sin(\bar{\omega}\tau)| = \frac{8\bar{b}^2\bar{\Upsilon}_1}{3\pi}\,\sin(\bar{\omega}\tau) = \frac{16}{3\pi^2}\,\frac{C_D\rho_w D_o L_c}{\gamma_v}\,\bar{b}^2\,\sin(\bar{\omega}\tau) \tag{C.12}$$

Direct comparison with the general expression of LC3:

$$\bar{F}(\tau) = \tilde{\bar{f}}\,\sin(\bar{\omega}\tau) \tag{C.13}$$

leads to:

$$\tilde{\bar{f}} = \frac{16}{3\pi^2}\,\frac{C_D\rho_w D_o L_c}{\gamma_v}\,\bar{b}^2 \tag{C.14}$$

It is worth noting that, differently from LC1 and LC2, LC3 inherently exhibit a non-dimensional forcing function $\tilde{\bar{f}}$ which is linearly depending on the drag coefficient of the tether C_D and quadratically depending on the non-dimensional base value of the water particle velocity $\bar{b}$.

At this stage, the proper external loading term has been linearized, while the nonlinear feedback term in the structural velocity still needs to be addressed.
To do so, the Harmonic Balance Method (HBM) is used. The HBM, in its essence, consists in finding an equivalent linear system which possesses the same steady-state vibration amplitude as the initial non-linear one.

Since the objective is to linearize just the feedback term in the structural velocity, the equation of motion to be preliminary considered is the fixed-supports equation of motion of the tether, without geometrical nonlinearities, in its dimensionless version:

$$\ddot{\bar{z}} + \bar{\omega}^2\bar{z} = -\bar{\Upsilon}_2\,|\bar{z}'(\tau)|\bar{z}'(\tau) \tag{C.15}$$

while the desired linear equation reads:

$$\ddot{\bar{z}} + \bar{c}^{eq}\,\dot{\bar{z}} + \bar{k}^{eq}\,\bar{z} = 0 \tag{C.16}$$

$\bar{c}^{eq}$ and $\bar{k}^{eq}$ being non-dimensional equivalent damping and stiffness coefficients, respectively. Recalling Eq. (C.8), the righthand side of Eq. (C.15) can be cast in the following dimensionless form:

$$\bar{F}(\tau) = -\bar{a}^2\bar{\omega}^2\bar{\Upsilon}_2\,\sin\Theta|\sin\Theta| \tag{C.17}$$

Standard integrals allow to express Eq. (C.17) by means of its Fourier representation:

$$\bar{F}(\tau) = -\frac{8\bar{a}^2\bar{\omega}^2\bar{\Upsilon}_2}{3\pi}\,\sin\Theta \tag{C.18}$$

At this stage, an equivalent linear dimensionless forcing can be defined as:

$$\bar{F}_1 = \bar{k}_1\,\bar{z} + \bar{c}^{eq}\,\bar{z}' = \bar{k}_1\,\bar{a}\,\cos\Theta - \bar{\omega}\,\bar{c}^{eq}\,\bar{a}\,\sin\Theta \tag{C.19}$$

with $\bar{k}_1 = \bar{k}^{eq} - \bar{\omega}^2$. Direct comparison of Eqs. (C.18) and (C.19) leads to the following conditions:

$$\bar{k}_1\bar{a} = 0 \implies \bar{k}_1 = 0 \tag{C.20}$$

$$-\bar{\omega}\,\bar{c}^{eq}\,\bar{a} = -\frac{8\,\bar{a}^2\bar{\omega}^2\bar{\Upsilon}_2}{3\pi} \implies \bar{c}^{eq} = \frac{8\,\bar{a}\,\bar{\omega}\,\bar{\Upsilon}_2}{3\pi} \tag{C.21}$$

Therefore, the resulting linear system is characterized by an equivalent non-dimensional stiffness which is the same as the original non-linear one (i.e. $\bar{k}^{eq} = \bar{\omega}^2$) and possesses an equivalent non-dimensional damping coefficient expressed by Eq. (C.21). The equivalent viscous damping coefficient is amplitude-dependent and reads:

$$\xi^{eq}(\bar{a}) = \frac{\bar{c}^{eq}}{2\,\bar{\omega}} = \frac{8\,\bar{\Upsilon}_2}{3\pi\,\gamma_v\,L_0}\,\bar{a} \tag{C.22}$$

Direct substitution of Eq. (C.11) into Eq. (C.22) leads to:

$$\xi^{eq}(\bar{a}) = \frac{16}{9\pi^2}\,\frac{C_D\,\rho_w\,D_o\,L_c}{\gamma_v}\,\bar{a} \tag{C.23}$$

The following “equivalent damping” non-dimensional coefficient is hence introduced:

$$\bar{K}_d = \frac{16}{9\pi^2}\,\frac{C_D\,\rho_w\,D_o\,L_c}{\gamma_v} \tag{C.24}$$

The total viscous damping coefficient of the structure then reads:

$$\xi(\bar{a}) = \xi^s + \xi^{eq}(\bar{a}) = \xi^s + \bar{K}_d\,\bar{a} \tag{C.25}$$

The non-dimensional equation of motion of the fixed-supports tether (LC3), in the spirit of the perturbation approach, finally becomes:

$$\ddot{\bar{z}}(\tau) + 2(\xi^s + \xi^{eq})\bar{\omega}\dot{\bar{z}}(\tau) + \bar{\omega}^2\bar{z}(\tau) + 3\bar{\beta}\bar{z}^2(\tau) + \bar{\nu}\bar{z}^3(\tau) = \tilde{\bar{f}}\,\sin[\bar{\omega}\,(1+\Delta)\,\tau] \tag{C.26}$$

where $\tilde{\bar{f}}$ and ξ^{eq} are respectively given by Eqs. (C.14) and (C.23).

References

[1] R. Bruschi, V. Giardinieri, R. Marazza, T. Merletti, Submerged buoyant anchored tunnels: technical solutions for the fixed link across the Strait of Messina, Italy, in: J. Krokeborg (Ed.), Strait Crossings, Balkema, Rotterdam, 1990, pp. 605–612.
[2] T. Fujii, Submerged floating tunnel in funka bay design and execution, in: Proc. Int. Conf. Submerg. Float. Tunn., Sandnes, Norway, 1996, pp. 90–111.
[3] P. Fogazzi, F. Perotti, The dynamic response of seabed anchored floating tunnels under seismic excitation, Earthq. Eng. Struct. Dyn. 29 (2000) 273–295.
[4] F.M. Mazzolani, R. Landolfo, B. Faggiano, M. Esposto, F. Perotti, G. Barbella, Structural analyses of the submerged floating tunnel prototype in Qiandao lake (PR of China), Adv. Struct. Eng. 11 (2008) 439–454.
[5] S. Kanie, Feasibility studies on various SFT in Japan and their technological evaluation, Procedia Eng. 4 (2010) 13–20.
[6] B. Jakobsen, Design of the submerged floating tunnel operating under various conditions, Procedia Eng. 4 (2010) 71–79.
[7] W. Xu, Y. Ma, G. Liu, M. Li, A. Li, M. Jia, Z. He, Z. Du, et al., A review of research on tether-type submerged floating tunnels, Appl. Ocean Res. 134 (2022) 103525: 1–27.
[8] I.W.G. for Immersed, F. Tunnels, An Owner's Guide to Submerged Floating Tunnels, ITA Report 33, International Tunnelling and Underground Space Association, 2023.
[9] A. Nasr, I. Björnsso, D. Honfi, O.L. Ivanov, J. Johansson, E. Kjellström, A review of the potential impacts of climate change on the safety and performance of bridges, Sustain. Resilient Infrastruct. 6 (3–4) (2021) 192–212.
[10] W.G.S. tube bridges, Guidelines for Submerged Floating Tube Bridges. Guide to good practice, Technical Report fib Bulletin 96, Fédération internationale du béton (fib), 2020.
[11] B. Jiang, B. Liang, Study on the main influence factors of traffic loads in dynamic response of submerged floating tunnels, Procedia Eng. 166 (2016) 171–179.
[12] M. Shahmardani, Moving load analysis of submerged floating tunnels, Int. J. Eng. Trans. C: Asp. 25 (1) (2012) 17–24.
[13] H. Lin, Y. Xiang, Y. Yang, et al., Vehicle-tunnel coupled vibration analysis of submerged floating tunnel due to tether parametric excitation, Mar. Struct. 67 (2019) 102646: 1–14.
[14] G.A. Torres-Alves, C.M.P. Hart, O. Morales-Napoles, S.N. Jonkman, et al., Structural reliability analysis of a submerged floating tunnel under copula-based traffic load simulations, Eng. Struct. 269 (2022) 114752: 1–19.
[15] Y. Yang, Y. Xiang, C. Gao, et al., Vehicle-SFT-current coupling vibration of multi-span submerged floating tunnel, Part I: mode superposition and Galerkin hybrid method, Ocean Eng. 247 (2022) 110746: 1–18.
[16] Y. Yang, Y. Xiang, C. Gao, et al., Vehicle-SFT-current coupling vibration of multi-span submerged floating tunnel, Part II: comparative analysis of finite difference method and parametric study, Ocean Eng. 249 (2022)110951: 1–18.
[17] C. Jin, M.H. Kim, Tunnel-mooring-train coupled dynamic analysis for submerged floating tunnel under wave excitations, Appl. Ocean Res. 94 (2020) 102008.
[18] M. Di Pilato, A. Feriani, F. Perotti, et al., Numerical models for the dynamic response of submerged floating tunnels under seismic loading, Earthq. Eng. Struct. Dyn. 37 (2008) 1203–1222.
[19] L. Martinelli, G. Barbella, A. Feriani, et al., Modeling of Qiandao lake submerged floating tunnel subject to multi-support seismic input, Procedia Eng. 4 (2010) 311–318.
[20] G. Martire, B. Faggiano, M. Esposto, F.M. Mazzolani, A. Zollo, T.A. Stabile, Seismic analysis of a SFT solution for the Messina Strait crossing, Procedia Eng. 4 (2010) 303–310.
[21] J.H. Lee, S.I. Seo, H.S. Mun, et al., Seismic behaviors of a floating submerged tunnel with a rectangular cross-section, Ocean Eng. 127 (2016) 32–47.
[22] L. Martinelli, M. Domaneschi, C. Shi, et al., Submerged floating tunnels under seismic motion: vibration mitigation and seaquake effects, Procedia Eng. 166 (2016) 229–246.
[23] J. Mirzapour, M. Shahmardani, S. Tariverdilo, et al., Seismic response of submerged floating tunnel under support excitation, Sh. Offshore Struct. 12 (2017) 404–411.
[24] J. Lee, C. Jin, M. Kim, et al., Dynamic response analysis of submerged floating tunnels by wave and seismic excitations, Ocean Syst. Eng. 7 (2017) 1–19.
[25] C. Jin, M.H. Kim, Time-Domain hydro-elastic analysis of a SFT (submerged floating tunnel) with mooring lines under extreme wave and seismic excitations, Appl. Sci. 8 (2018) 2386: 1–18.
[26] K. Wang, G.K. Er, V.P. Iu, et al., Nonlinear random vibrations of moored floating structures under seismic and sea wave excitations, Mar. Struct. 65 (2019) 75–93.
[27] F. Foti, L. Martinelli, F. Perotti, SFTs under seismic loading: conceptual design and optimization tools, in: H. Yokota, D.M. Frangopol (Eds.), Bridge Maintenance, Safety, Management, Life-Cycle Sustainability and Innovations (IABMAS 2020), CRC Press, London, 2020, pp. 837–843.
[28] F. Foti, L. Martinelli, F. Perotti, A semi-analytical model for the design and optimization of SFTs under seismic loading, in: J. Ramon Casas, D.M. Frangopol, J. Turmo (Eds.), Bridge Safety, Maintenance, Management, Life-Cycle, Resilience and Sustainability (IABMAS 2022), CRC Press, London, 2022, pp. 1117–1121.
[29] J. Xie, J. Li, J. Chen, Q. Xu, Seismic response analysis of submerged floating tunnel considering non-uniform excitation and flexible-support boundary effect, Ocean Eng. 286 (2023) 115486.
[30] S. Corazza, M. Geuzaine, F. Foti, V. Denoël, L. Martinelli, On the seismic response of anchoring elements for submerged floating tunnels, in: V. Gattulli, M. Lepidi, L. Martinelli (Eds.), Lecture Notes in Civil Engineering, 399 of *Dynamics and Aerodynamics of Cables*, Springer Nature, 2023, pp. 303–313.
[31] M. Xiong, Z. Chen, Y. Huang, et al., Nonlinear stochastic seismic dynamic response analysis of submerged floating tunnel subjected to non-stationary ground motion, Int. J. Non-Linear Mech. 148 (2023) 104270: 1–12.
[32] W. Chen, Y. Li, Y. Fu, S. Guo, On mode competition during VIVs of flexible SFT's flexible cylindrical body experiencing lineally sheared current, Procedia Eng. 166 (2016) 201–290.
[33] Y. Hong, F. Ge, Dynamic response and structural integrity of submerged floating tunnel due to hydrodynamic load and accidental load, Procedia Eng. 4 (2010) 35–50.

[34] H. Kunisu, Evaluation of wave force acting on submerged floating tunnels, Procedia Eng. 4 (2010) 99–105.
[35] S.I. Seo, H.S. Mun, J.H. Lee, J.H. Kim, et al., Simplified analysis for estimation of the behavior of a submerged floating tunnel in waves and experimental verification, Mar. Struct. 44 (2015) 142–158.
[36] Z. Chen, Y. Xiang, H. Lin, Y. Yang, et al., Coupled vibration analysis of submerged floating tunnel system in wave and current, Appl. Sci. 8 (2018) 1311: 1–14.
[37] X. Long, F. Ge, L. Wang, Y. Hong, Effects of fundamental structure parameters on dynamic responses of submerged floating tunnel under hydrodynamic loads, Acta Mech. Sin. 25 (3) (2009) 335–344.
[38] X. Long, F. Ge, Y. Hong, Feasibility study on buoyancy–weight ratios of a submerged floating tunnel prototype subjected to hydrodynamic loads, Acta Mech. Sin. 31 (5) (2015) 750–761.
[39] M. Di Pilato, F. Perotti, P. Fogazzi, et al., 3D dynamic response of submerged floating tunnels under seismic and hydrodynamic excitation, Eng. Struct. 30 (2008) 268–281.
[40] X. Chen, Q. Chen, Z. Chen, S. Cai, X. Zhuo, J. Lv, et al., Numerical modeling of the interaction between submerged floating tunnel and surface waves, Ocean Eng. 220 (2021) 108494: 1–16.
[41] S.B. Patil, D. Karmakar, Hydrodynamic analysis of floating tunnel with submerged rubble mound breakwater, Ocean Eng. 264 (2022) 112460: 1–18.
[42] P.X. Zou, J.D. Bricker, L.Z. Chen, W.S.J. Uijttewaal, C.S. Ferreira, et al., Response of a submerged floating tunnel subject to flow-induced vibration, Eng. Struct. 253 (2022) 113809: 1–15.
[43] H. Zhang, Z. Yang, J. Li, C. Yuan, M. Xie, H. Yang, H. Yin, et al., A global review for the hydrodynamic response investigation method of submerged floating tunnels, Ocean Eng. 225 (2021) 108825: 1–13.
[44] C. Jin, M.H. Kim, J. Choi, W.S. Park, Coupled dynamics simulation of submerged floating tunnel for various system parameters and wave conditions, in: International Conference on Offshore Mechanics and Arctic Engineering, 51265, American Society of Mechanical Engineers, 2018.
[45] P.X. Zou, L.Z. Chen, The coupled tube-mooring system SFT hydrodynamic characteristics under wave excitations, in: E.J. Sapountzakis, M. Banerjee, P. Biswas, E. Inan (Eds.), Proceedings of the 14th International Conference on Vibration Problems, Springer Nature, Singapore, 2021, pp. 907–923.
[46] Z. Yang, J. Li, H. Zhang, C. Yuan, H. Yang, Experimental study on 2D motion characteristics of submerged floating tunnel in waves, J. Mar. Sci. Enigineering 8 (123) (2016) 18.
[47] Z. Yang, J. Li, Y. Xu, X. Ji, Z. Sun, Q. Ouyang, H. Zhang, et al., Experimental study on the wave-induced dynamic response and hydrodynamic characteristics of a submerged floating tunnel with elastically truncated boundary condition, Mar. Struct. 88 (2023) 103339: 1–21.
[48] Z. Wu, D. Wang, W. Ke, Y. Qin, F. Lu, M. Jiang, et al., Experimental investigation for the dynamic behavior of submerged floating tunnel subjected to the combined action of earthquake, wave and current, Ocean Eng. 239 (2021) 109911: 1–19.
[49] T. Liu, T. Viuff, B.J. Leira, X. Xiang, A. Minoretti, K.H. Halse, et al., Response validation of a submerged floating tunnel segment, Ocean Eng. 264 (2022) 112396: 1–14.
[50] P.X. Zou, Dynamic Response of a Submerged Floating Tunnel Subject to Hydraulic Loading. Numerical Modelling for Engineering Design, Ph.D. thesis, TU Delft, Delft Universiy of Technology, 2022.
[51] G. Iovane, F.M. Mazzolani, R. Landolfo, E. Begovic, E. Bilotta, B. Faggiano, Assessment of experimental tests on SFT small scale specimen, Appl. Ocean Res. 138 (2023) 103656:1–20.
[52] J.R. Morison, J.W. Johnson, S.A. Schaaf, The force exerted by surface waves on piles, J. Pet. Technol. 2 (5) (1950) 149–154.
[53] F. Foti, L. Martinelli, E. Morleo, F. Perotti, Dynamic response of submerged floating tunnels: an enhanced semi-analytical approach, Ocean Eng. 294 (2024) 116648: 1–14.
[54] S. Corazza, F. Foti, L. Martinelli, Dynamic substructuring technique for submerged floating tunnels, in: J.S. Jensen, D.M. Frangopol, J.W. Schmidt (Eds.), Bridge Maintenance, Safety, Management, Digitalization and Sustainability, CRC Press/Balkema, 2024, pp. 1029–1036.
[55] D. Cantero, A. Rønnquist, A. Naess, et al., Recent studies of parametrically excited mooring cables for submerged floating tunnels, Procedia Eng. 166 (2016) 99–106.
[56] P. Warnitchai, Y. Fujino, T. Susumpow, A non-linear dynamic model for cables and its application to a cable-structure system, J. Sound Vib. 187 (4) (1995) 695–712.
[57] J.F. Wilson, Dynamics of Offshore Structures, Wiley Inc, Hoboken, 1984.
[58] S.K. Chakrabarti, Hydrodynamics of Offshore Structures, in: Computational Mechanics Publications, Springer, Berlin, 1987.
[59] C.L. Bretschneider, Wave Variability and Wave Spectra for Wind-Generated Gravity Waves, Technical memorandum, United States, Beach Erosion Board, Corps of Engineers, 1959.
[60] S. Corazza, F. Foti, L. Martinelli, V. Denoël, Global and local response of SUubmerged floating tunnels to hydrodynamic loads, in: ASME (Ed.), Proceedings of the ASME 2025 44th International Conference on Ocean, Offshore and Arctic Engineering, Vol. 1: Offshore Technology; Structures, Safety and Reliability; Materials Technology, Vancouver, Canada, 2025.
[61] T. Sarpkaya, M. Isaacson, Mechanics of Wave Forces on Offshore Structures, 1st Edition, Van Nostrand Reinhold Company, 1981.
[62] X. Li, S. Quek, C. Koh, Stochastic response of offshore platforms by statistical cubicization, J. Eng. Mech. 121 (10) (1995) 1056–1068.
[63] M.A. Tognarelli, A. Kareem, Equivalent statistical cubicization for system and forcing nonlinearities, J. Eng. Mech. 123 (8) (1997) 890–893.
[64] V. Volterra, Theory of Functionals and of Integral and Integro-Differential Equations, Dover Publications, Inc., New York, USA, 1959.
[65] M. Schetzen, The Volterra and Wiener Theories of Nonlienear Systems, Krieger Publishing Company, 2006.
[66] H. Irvine, Cable Structures, MIT Press Series in Structural Mechanics, 1981.
[67] A.H. Nayfeh, Perturbation Methods, Wiley-VCH Verlag GmbH & Co. KGaA, 2004.
[68] A.H. Nayfeh, Nonlinear Oscillations, John Wiley & Sons, Inc., 1995.
[69] O.M. Faltinsen, Sea Loads on Ships and Offshore Structures, Cambridge, Cambridge University Press, 1990.
[70] T. Canor, V. Denoël, On the influence of background component in resonance of cables, in: Proceedings of the 9th International Symposium on Cable Dynamics (ISCD 2011), Shangai, China, 2011.
[71] E.J. Hinch, Perturbation Methods, Cambridge University Press, 1991.
[72] A.H. Nayfeh, Introduction to Perturbation Techniques, John Wiley & Sons, 1993.
[73] M. Azimi, Stability and bifurcation of Mathieu–Duffing equation, Int. J. Non-Linear Mech. 144 (2022) 104049: 1–14.
[74] A.A. Barakat, E.M. Weig, P. Hagedorn, Non-trivial solutions and their stability in a two-degree-of-freedom Mathieu–Duffing system, Nonlinear Dyn. 111 (2023) 22119–22136.
[75] C.S. Hsu, The response of a parametrically excited hanging string in fluid, J. Sound Vib. 39 (3) (1975) 305–316.
[76] I.K. Chatjigeorgiou, S.A. Mavrakos, Nonlinear resonances of parametrically excited risers—numerical and analytic investigation for $\Omega = 2\omega_1$, Comput. Struct. 83 (2005) 560–573.
[77] G.R. Franzini, C.E.N. Mazzilli, Non-linear reduced-order model for parametric excitation analysis of an immersed vertical slender rod, Int. J. Non-Linear Mech. 80 (2016) 29–39.
[78] G.J. Vernizzi, S. Lenci, G.R. Franzini, A detailed study of the parametric excitation of a vertical heavy rod using the method of multiple scales, Meccanica 55 (2020) 2423–2437.